



# The Role of Kinetic Instabilities and Waves in Collisionless Magnetic Reconnection

D.B. Graham<sup>1</sup> · G. Cozzani<sup>2</sup> · Yu.V. Khotyaintsev<sup>1,3</sup> · V.D. Wilder<sup>4</sup> · J.C. Holmes<sup>5</sup> · T.K.M. Nakamura<sup>6</sup> · J. Büchner<sup>7,8</sup> · K. Dokgo<sup>9</sup> · L. Richard<sup>1</sup> · K. Steinvall<sup>10</sup> · C. Norgren<sup>1,11</sup> · L.-J. Chen<sup>12</sup> · H. Ji<sup>13,14</sup> · J.F. Drake<sup>15</sup> · J.E. Stawarz<sup>16</sup> · S. Eriksson<sup>17</sup>

Received: 6 June 2024 / Accepted: 18 December 2024 / Published online: 14 February 2025  
© The Author(s) 2025

## Abstract

Magnetic reconnection converts magnetic field energy into particle energy by breaking and reconnecting magnetic field lines. Magnetic reconnection is a kinetic process that generates a wide variety of kinetic waves via wave-particle interactions. Kinetic waves have been proposed to play an important role in magnetic reconnection in collisionless plasmas by, for example, contributing to anomalous resistivity and diffusion, particle heating, and transfer of energy between different particle populations. These waves range from below the ion cyclotron frequency to above the electron plasma frequency and from ion kinetic scales down to electron Debye length scales. This review aims to describe the progress made in understanding the relationship between magnetic reconnection and kinetic waves. We focus on the waves in different parts of the reconnection region, namely, the diffusion region, separatrices, outflow regions, and jet fronts. Particular emphasis is placed on the recent observations from the Magnetospheric Multiscale (MMS) spacecraft and numerical simulations, which have substantially increased the understanding of the interplay between kinetic waves and reconnection. Some of the ongoing questions related to waves and reconnection are discussed.

**Keywords** Magnetic reconnection · Waves · Instabilities · Kinetic processes · Methods

## 1 Introduction

Magnetic reconnection is the process by which magnetic field lines break and reconnect, resulting in explosive energy releases in the form of particle acceleration and heating (Yamada et al. 2010). Magnetic reconnection is a fundamental process in solar and astrophysical plasmas, and occurs in many plasma environments, such as planetary magnetopauses and magnetotails, the solar corona, the solar wind, and accretion disks. In many contexts, such as at Earth's magnetopause and magnetotail, magnetic reconnection is essentially a collisionless process (Coulomb collisions do not play a significant role). As a result, particle distributions can deviate significantly from Maxwellian distributions, resulting in unstable particle distributions and leading to a wide variety of plasma waves and instabilities. Additionally, the strong currents and plasma inhomogeneities associated with magnetic reconnection pro-

vide a source of energy for waves. Through wave-particle interactions, waves can modify the local plasma and have important effects on reconnection. For example, waves can heat the plasma, dissipate currents, produce anomalous resistivity and diffusion, and can transfer energy between different particle species. These effects can have important consequences for ongoing reconnection. Likewise, pre-existing waves in the plasma could impact the initialization of reconnection.

The waves associated with magnetic reconnection have been studied extensively using spacecraft observations, laboratory experiments, and numerical simulations. These different approaches have each provided insights into the role waves play in magnetic reconnection. In the case of spacecraft observations, high-resolution measurements of the electric and magnetic fields have enabled waves to be directly characterized and studied, while particle measurements with much lower time resolution than that of the fields have made determining the cause and effects of waves on the plasma challenging. Simulations can model the large-scale reconnection processes along with the development of kinetic waves. However, to achieve this, artificial or idealized plasma conditions often need to be employed.

The relationship between kinetic waves and reconnection has been reviewed several times in the past (Vaivads et al. 2006; Fujimoto et al. 2011; Khotyaintsev et al. 2019). These reviews have shown that important advances have been made using spacecraft observations, such as Cluster, THEMIS (Time History of Events and Macroscale Interactions during Substorms), and MMS (Magnetospheric Multiscale), numerical simulations, and laboratory experiments. Ji et al. (2023) provides a recent review of laboratory experiments on collisionless reconnection, including the associated waves.

The aim of this paper is to review the most recent advances in our understanding of the relation between magnetic reconnection and kinetic plasma waves. We primarily focus on recent in situ observations from the MMS spacecraft and recent numerical simulations. The outline of this paper is as follows: Sect. 2 provides an overview of magnetic reconnection and the associated waves. In Sect. 3, we describe the waves associated with the different regions of reconnection, namely, the diffusion region, separatrices, outflow regions, and jet fronts. In Sect. 4, we focus on larger-scale instabilities, namely, current sheet kinking and tearing mode instabilities, and their interaction with reconnection. In Sect. 5, we discuss the effects of waves on reconnection and ongoing questions. In Sect. 6, we state the conclusions and recent key results.

## 2 Overview of Waves and Reconnection

In this section, we provide an overview of the waves associated with reconnection. In particular, we describe the types of waves that have been reported and where they are found in relation to the different regions of magnetic reconnection.

Plasmas consist of ions and electrons and are governed by electromagnetic forces acting collectively on the particles. Waves in plasmas are generally defined as oscillations in the electromagnetic fields and particles, which propagate in a plasma and can transport energy without net motion of the plasma. Waves develop in a plasma due to instabilities, which result from free energy that has accumulated in the system. The theory of plasma waves and instabilities has been studied in many papers and textbooks. Comprehensive reviews of the theory of plasma waves and instabilities can be found in Stix (1992), Swanson (1989), Treumann and Baumjohann (1997), Gary (1993).

In magnetic reconnection, and plasmas more generally, there are multiple sources of free energy. These include deformations in the particle distribution functions, inhomogeneities in the plasma, and electric currents. The effect of the growing waves on the plasma is to remove the free energy responsible for the generation of the waves. This can include returning unstable particle distributions to stable distributions, reducing the magnitude of electric currents, and reducing inhomogeneities in the plasma. Additionally, plasma waves can potentially produce anomalous resistivity and diffusion, as well as heat the plasma through wave-particle interactions. Waves can also potentially accelerate particles to non-thermal energies.

In plasmas, waves can be either electrostatic or electromagnetic. Electrostatic waves are characterized by longitudinal fluctuations in the electric field  $\mathbf{E}$ , namely  $\mathbf{E}$  is aligned with the wave vector  $\mathbf{k}$ , due to charge separation and have no associated magnetic field  $\mathbf{B}$  fluctuations. Examples of electrostatic waves include Langmuir waves, ion-acoustic waves, and electron-acoustic waves. Electromagnetic waves are characterized by  $\mathbf{E}$  transverse to the wave vector  $\mathbf{k}$  and have associated magnetic field fluctuations. Examples of electromagnetic waves include magnetic field  $\mathbf{B}$  aligned whistler and Alfvén waves. In general, waves exhibit both electrostatic and electromagnetic components, but are classified as electrostatic or electromagnetic depending on which component of  $\mathbf{E}$  dominates.

In magnetic reconnection regions, a wide variety of waves can develop. Table 1 lists some of the most common waves associated with magnetic reconnection, along with their properties and the sources of instability. The different plasma waves span multiple spatial scales and frequencies. At relatively low frequencies, close to the ion cyclotron frequency  $f_{ci}$ , Alfvén or ion-cyclotron waves can develop due to deformations in the ion particle distribution functions. At smaller scales between ion and electron spatial scales, lower hybrid waves can develop. Electron-scale waves include Langmuir and upper hybrid (UH) waves, ion-acoustic waves, and whistler waves.

Figure 1 provides a schematic overview of the different regions associated with magnetic reconnection, namely, the ion and electron diffusion regions, separatrices, outflow regions, and jet fronts. Magnetic reconnection is often characterized by an X-line magnetic field structure, where the magnetic fields associated with inflowing plasmas reconnect. The separatrix regions are narrow boundaries between the inflow and outflow regions. Near the X line are the ion and electron diffusion regions, where ions and electrons, respectively, decouple from the magnetic field (shown in red and blue). In each of these regions, different types of electrostatic and electromagnetic waves commonly develop, some of which are listed in Table 1. Figure 1 represents symmetric reconnection, where the inflowing plasmas have the same properties. Symmetric reconnection typically occurs in Earth's magnetotail. In contrast, reconnection is typically asymmetric at Earth's dayside magnetopause, where reconnection occurs between the hotter tenuous magnetospheric and the cooler, denser magnetosheath plasmas. These different plasma conditions modify the ion and electron distributions observed in the separatrices, outflow regions, and diffusion regions, which can modify the types of instabilities that develop. Additionally, the out-of-plane guide field can vary for reconnection, which can modify the structure and dynamics of the diffusion region. In particular, for a negligible guide field, the currents around the electron diffusion region (EDR) are perpendicular to  $\mathbf{B}$ , while for a strong guide field, strong currents parallel to  $\mathbf{B}$  occur. This, too, can modify the types of instabilities that can develop. In the following section, we discuss the differences between symmetric and asymmetric reconnection, and antiparallel and guide-field reconnection, where applicable.

**Table 1** A summary of some of the commonly observed waves associated with magnetic reconnection. The properties of the waves and the sources of free energy

Summary of the most common waves associated with magnetic reconnection		
Waves	Properties and observed characteristics	Source of the waves
Langmuir waves	Electrostatic waves with narrow frequency range near $f_{pe}$ , with $E_{\parallel} \gg E_{\perp}$ .	Fast electron beams; bump-on-tail instability.
Upper hybrid waves	Quasi-electrostatic waves with narrow range near $f_{uh}$ , with $E_{\perp} \gg E_{\parallel}$ .	Complex electron distributions such as beams, loss cones, and agyrotropic distributions.
Electron holes	Nonlinear localized positive potential structures supported by trapped electrons. Seen as bipolar fluctuations in $E_{\parallel}$ .	Nonlinear evolution of streaming instabilities, such as from electron beams and relative drift between electron and ion populations.
Ion-acoustic waves	Electrostatic waves with frequencies near $f_{pi}$ . Typically $E_{\parallel} \gg E_{\perp}$ .	Relative drift between electron and ion populations and ion beams. Typically occur when $ZT_e \gg T_i$ .
Whistler waves	Typically electromagnetic waves with right-hand circular polarization and frequencies $f_{lh} \lesssim f < f_{ce}$ . Identified from ellipticity of $\mathbf{B}$ fluctuations.	Electron temperature anisotropy $T_{\perp} > T_{\parallel}$ , loss cones, electron beams, parallel electron heat flux.
Lower hybrid waves	Typically quasi-electrostatic waves with measurable $\mathbf{B}$ fluctuations and frequencies near $f_{lh}$ .	Plasma inhomogeneities and cross-field currents, relative drift between electron and ions or different ion populations in the cross-field direction.
Alfvén waves	Magnetic field fluctuations near $f_{ci}$ , often left-hand polarization.	Ion temperature anisotropies $T_{\perp} > T_{\parallel}$ , ion beams.

### 3 Regions of Reconnection

In this section, we review the different types of waves associated with magnetic reconnection. We focus on the different regions associated with reconnection, namely, the diffusion region, separatrix regions, outflow regions, and jet fronts.

#### 3.1 Diffusion Region

A wide variety of waves have been reported in or near reconnection diffusion regions. In the ion diffusion region (IDR), ion meandering and finite Larmor radius effects occur, leading to agyrotropic ion crescent-shaped distributions. Similarly, agyrotropic electron distributions occur in the EDR due to finite Larmor radius effects. In the diffusion region, strong currents and plasma inhomogeneities also develop. All these features can lead to the development of a wide variety of plasma waves. Before MMS, diffusion regions, in particular EDRs, were difficult to identify. Therefore, observations of waves associated with diffusion regions are biased toward MMS observations. Recent research has particularly focused on the nature of lower hybrid drift waves near the diffusion region and UH and electron Bernstein waves in the EDR.



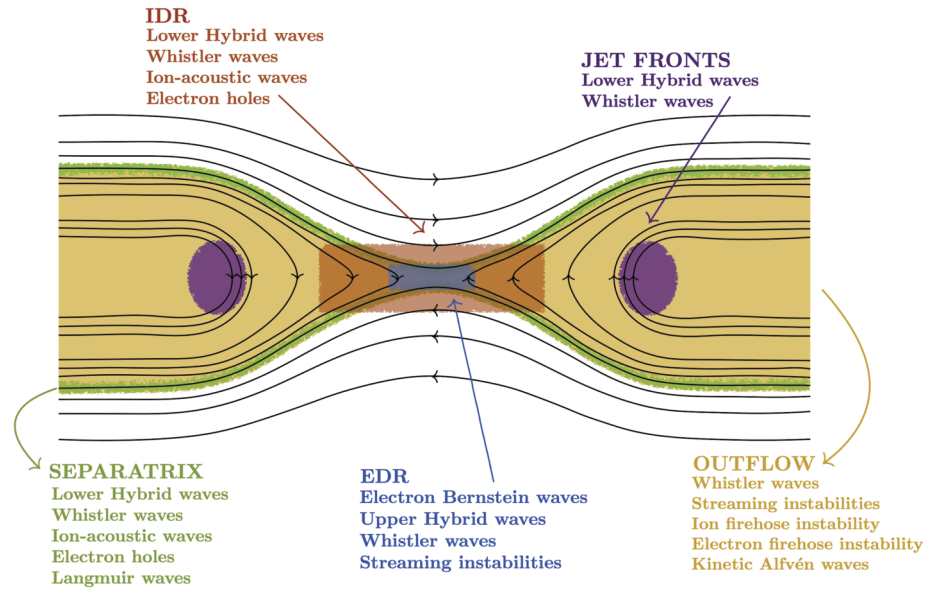


**Fig. 1** Schematic of magnetic reconnection showing the different regions, namely, the ion and electron diffusion regions (red and blue), separatrices (green), ion outflow (yellow), and jet front regions (purple). For these regions we list the types of waves expected there based on observations and simulations

**Upper Hybrid and Electron Bernstein Waves** One of the first results from MMS observations was the verification of agyrotropic crescent-shaped or beam electron distributions in the EDR of symmetric (Torbert et al. 2018) and asymmetric reconnection (Burch et al. 2016). These distributions form due to electron finite Larmor radius effects or electron bouncing near the center of the current sheet (Norgren et al. 2016, 2025, this collection). At Earth's magnetopause these distributions have been observed on both the magnetospheric (Burch et al. 2016) and magnetosheath (Chen et al. 2016) side of the X line. Graham et al. (2017b) found intense UH waves associated with agyrotropic electron beams and crescent-shaped distributions on the magnetosheath side of the X line in the EDR. The source of the waves was a beam-plasma instability between the agyrotropic electron beam and the core population, where the beam component has been demonstrated to be unmagnetized meandering electrons (Chen et al. 2017). UH waves generated by agyrotropic electron distributions in the EDR were subsequently found by Burch et al. (2019) for symmetric reconnection in Earth's magnetotail due to the same beam-plasma instability.

Figures 2a–2c show an example of the UH waves observed at a magnetotail EDR by MMS3 (Burch et al. 2019). In this and the other events, the waves are characterized by  $E_{\perp} \gg E_{\parallel}$ , and the waves have frequency near  $f_{pe} \approx f_{uh}$ , where  $f_{pe}$  and  $f_{uh}$  are the electron plasma and upper hybrid frequencies. Like the magnetopause case, the source of instability was shown to be the agyrotropic crescent-shaped distributions. Figure 2c shows an example of the electron distribution observed at the same time as the UH waves. The distribution is characterized by a gyrotropic core population and a higher energy agyrotropic beam or crescent component. A later case study by Li et al. (2021) found that UH waves were generated on both inflow sides of the EDR in Earth's magnetotail. Li et al. (2021) argued that the waves were generated by inbound meandering electrons and that the waves could significantly dissipate energy from the electrons.

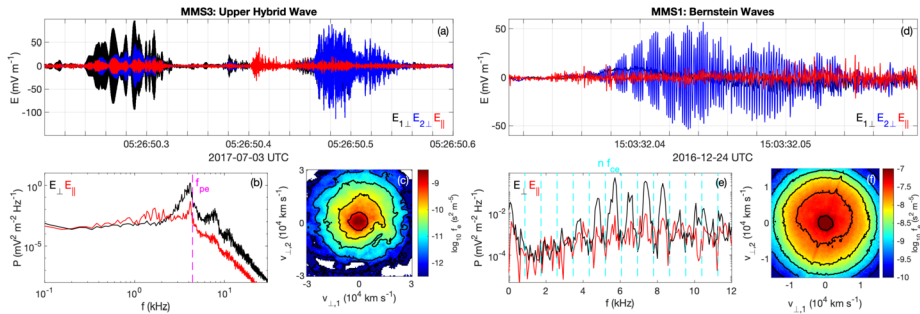


**Fig. 2** Example of upper hybrid (UH) waves observed by MMS in magnetotail reconnection, based on Burch et al. (2019) (panels a–c), and an example of electron Bernstein waves in magnetopause reconnection, based on Li et al. (2020) (panels d–f). (a) and (d) Electric field waveform of the UH waves and Bernstein waves, respectively. The waveforms are presented in field-aligned coordinates, where  $E_{1\perp}$  and  $E_{2\perp}$  (black and blue) are the electric field perpendicular to  $\mathbf{B}$ , while  $E_{\parallel}$  (red) is aligned with  $\mathbf{B}$ . (b) and (e) Power spectra of UH and Bernstein waves, respectively. The black and red lines are the powers of  $E_{\perp}$  and  $E_{\parallel}$ , respectively. In panel (b), the magenta dashed line indicates  $f_{pe}$ , and in panel (e), the cyan dashed line indicates  $f_{ce}$  and its harmonics. (c) and (f) Two-dimensional reduced electron distributions in the plane normal to  $\mathbf{B}$  at the times the waves were observed, where  $v_{\perp,2}$  is in the direction of bulk flow perpendicular to  $\mathbf{B}$ , and  $v_{\perp,1}$  is orthogonal to  $\mathbf{B}$  and  $v_{\perp,2}$

In an EDR at Earth's magnetopause, agyrotropic electron distributions were found by Li et al. (2020) to generate a series of electron Bernstein waves. Similar to the case in Graham et al. (2017a), the waves were observed on the magnetosheath side of the EDR. Figures 2d–2f show these Bernstein waves and the associated electron distribution. The Bernstein waves are characterized by  $E_{\perp} \gg E_{\parallel}$  and distinct spectral peaks at frequencies between the harmonics of the electron cyclotron frequency  $f_{ce}$ . The associated electron distribution, shown in Fig. 2f, exhibits a gyrotropic core population and an agyrotropic crescent-shaped component. Li et al. (2020) argued that the observed distributions could be unstable to electron Bernstein waves by modeling the agyrotropic crescent distributions as a gyrotropic ring distribution. In each case, the UH or Bernstein waves were associated with small to moderate guide-field reconnection events. To date, electron Bernstein waves have not been observed in magnetotail EDRs.

Crescent distributions are a key element of reconnection, and therefore recent theoretical and numerical results have focused on understanding the generation of the UH and Bernstein waves by agyrotropic distributions and the nonlinear evolution of the UH waves. Dokgo et al. (2020b) derived an electrostatic kinetic dispersion equation for an agyrotropic beam-plasma instability, which can model the growth of UH and electron Bernstein waves. Making use of the dispersion equation and plasma parameters obtained from MMS, they showed that this new model predicted that both types of waves could be excited, depending on the beam properties; when the beam was low density, the frequency of the excited waves was close to  $f_{pe}$ , while for denser beams the frequency was downshifted. For faster growth rates  $\gamma \gtrsim \Omega_{ce}$  a more continuous beam mode was found, while for lower growth rates discrete Bernstein modes became clearer. By comparing the model with observations from Li et al. (2020) and Burch et al. (2019) they were able to explain the generation of UH and Bernstein waves.

At present, fully kinetic three-dimensional simulations of reconnection, which can resolve these UH and Bernstein waves, are not possible due to the large separation in spatial and temporal scales. Instead, to numerically study these waves, small-scale local homogeneous simulations were performed using initial conditions and electron distributions based on MMS observations. Using these simulations, Dokgo et al. (2019) showed that UH waves

were generated by a beam-plasma interaction between the gyrotropic core electrons and agyrotropic beam. Moreover, the UH waves were found to undergo nonlinear processes, namely, the generation of electrostatic harmonic waves and the production of long-wavelength radio waves near  $f_{pe}$  and the second harmonic via nonlinear three-wave processes. Evidence of nonlinear electrostatic harmonics has been seen by MMS (Li et al. 2021) (see also Fig. 2b, where spectral peaks are observed at the harmonics of the UH waves). Similar simulations were employed to investigate how UH waves contribute to energy dissipation near the EDR (Dokgo et al. 2020a). Dokgo et al. (2020a) showed that the waves could contribute to dissipation via wave-particle interactions and argued that the profiles of plasma parameters could be modified due to the waves, which could affect the larger-scale energy dissipation processes in the EDR. Overall, these results show that the agyrotropic electron distributions in or near the EDR are often unstable to UH or Bernstein waves.

**Lower Hybrid Drift Waves** Lower hybrid waves are known to develop at plasma boundaries where the plasma is inhomogeneous. Thus, lower hybrid waves can develop at current sheets, in the IDR of reconnection, and along the separatrices. The waves are typically quasi-electrostatic and develop at short wavelengths with wave number  $k\rho_e \sim 1$ , where  $\rho_e$  is the electron Larmor radius, and develop at the edges of current sheets. However, near the center of the current sheet and close to the EDR, theory and simulations predict that lower hybrid waves become more electromagnetic with longer wavelengths, corresponding to  $k\sqrt{\rho_i\rho_e} \sim 1$  (Yoon et al. 2002; Daughton 2003), where  $\rho_i$  is the ion Larmor radius. In both cases, the waves tend to propagate in the reconnection out-of-plane direction with wave vectors nearly perpendicular to  $\mathbf{B}$ . In reconnection, the development of lower hybrid waves is most often attributed to the lower hybrid drift instability (Davidson et al. 1977), where inhomogeneities and cross-field currents drive the instability. Figure 3 shows two examples of three-dimensional (3D) magnetic reconnection where lower hybrid waves develop. The overall structure of the reconnection region is retained, while the lower hybrid waves introduce smaller-scale perturbations in the current density.

Lower hybrid waves are typically identified in spacecraft observations by electric field fluctuations, which exhibit broadband fluctuations around the lower hybrid frequency  $f_{lh}$  (Cattell and Mozer 1986). These fluctuations have been reported in the diffusion regions of reconnection at the magnetopause (Bale et al. 2002) and in the magnetotail (Zhou et al. 2009b). In some cases, the properties of the waves, such as wave vector and phase speed,

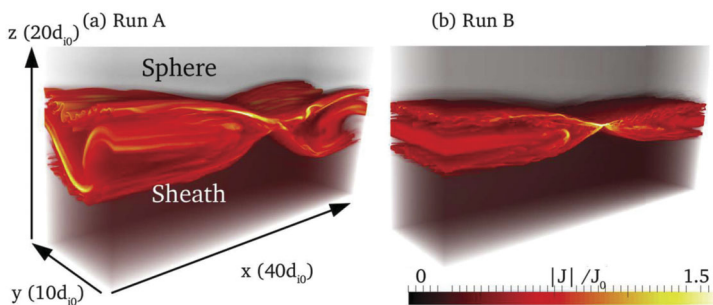


**Fig. 3** Volume rendering of current density from 3D PIC asymmetric reconnection simulations with different guide fields  $B_g$ . (a)  $B_g = 0.099 B_0$  (weak guide field); (b)  $B_g = 0.40 B_0$  (moderate guide field). The fluctuations at the separatrices are found in both runs and correspond to electrostatic lower hybrid waves. The run with a weak guide field also exhibits a longer-wavelength, electromagnetic lower hybrid mode, which is suppressed in higher guide-field simulations. Adapted from Le et al. (2018)

were determined using multi-spacecraft (Zhou et al. 2009b) and single-spacecraft methods (Norgren et al. 2012). Recent observations by MMS and numerical simulations have significantly improved our understanding of the behavior of the lower hybrid waves and their role in magnetic reconnection, owing to the high temporal resolution of the particle detectors and close tetrahedral configurations of the spacecraft.

At Earth's magnetopause, observations show that lower hybrid waves occur near the EDR and in the IDR, primarily on the low-density magnetospheric side of the X line (Bale et al. 2002; Graham et al. 2014; Khotyaintsev et al. 2016; Graham et al. 2017a, 2019). The electric field fluctuations are characterized by  $E_{\perp} \gg E_{\parallel}$ . The largest amplitude waves were primarily electrostatic, although magnetic field fluctuations associated with the waves occur (Carter et al. 2001; Graham et al. 2017a). As the center of the current sheet is approached, the waves tend to become more electromagnetic (Graham et al. 2019; Yoo et al. 2020). This was attributed to plasma becoming more weakly magnetized near the center of the current sheet (Graham et al. 2019; Yoo et al. 2020). However, close to the center of the current sheet, where the magnetic field is small, the amplitude of lower hybrid waves is significantly reduced (Graham et al. 2019, 2022), which suggests that the waves do not play a significant role in the EDR (Graham et al. 2022).

These results are consistent with recent 3D simulations of asymmetric magnetic reconnection, where intense lower hybrid waves were found in the low-density side of the X line (Roytershteyn et al. 2012; Price et al. 2016, 2017). In some simulations, the power of lower hybrid waves was reduced in the diffusion region compared with the separatrices (Pritchett 2013; Le et al. 2017; Price et al. 2020). However, this has not been clearly seen in observations, where large-amplitude lower hybrid waves have been reported both in the IDR and separatrices.

The presence of cold magnetospheric ions can also be a source of lower hybrid waves. Graham et al. (2017a) found that the relative drift between cold magnetospheric ions and finite Larmor radius magnetosheath ions in the magnetospheric inflow region can generate lower hybrid waves. Similarly, the relative cross-field drift between finite Larmor radius ions and electrons can excite lower hybrid waves via the modified two-stream instability (Graham et al. 2019).

Lower hybrid waves have also been observed close to the EDR during symmetric reconnection in the Earth's magnetotail. Chen et al. (2020) reported MMS observations of lower hybrid waves associated with electron heating and vortical flows at the EDR in an electron-scale current sheet. The observed lower hybrid waves are electron-scale fluctuations ( $k_{\perp} \rho_e \sim 1$ , where  $k_{\perp}$  is the wave number perpendicular to the ambient magnetic field) and propagate along the outflow direction. The wave electric field is so strong that the higher-energy electrons are demagnetized and gain energy through the wave potential, while the lower-energy electrons execute the  $E \times B$  vortical flow generating a magnetic field comparable to the guide field strength. This event was characterized by a moderate guide field (about 30% of the asymptotic reconnecting magnetic field component), which allows lower hybrid waves with a significant electrostatic component to be present in the center of the current sheet. The observations by Chen et al. (2020) suggest that electron dynamics in the reconnection layer can be modified by the waves.

Cozzani et al. (2021) presented observations of the electromagnetic long-wavelength lower hybrid mode ( $k \sqrt{\rho_i \rho_e} \sim 2.7$ ) in the magnetotail electron-scale current layer with weak guide field (see Figs. 4a–4f). Large-amplitude oscillations of the electron-scale gradients at the separatrix immediately adjacent to the EDR and magnetic-field fluctuations at the center of the current sheet reveal the presence of the electromagnetic drift instability leading to the current sheet kinking. The observed properties of the waves are consistent with the obliquely

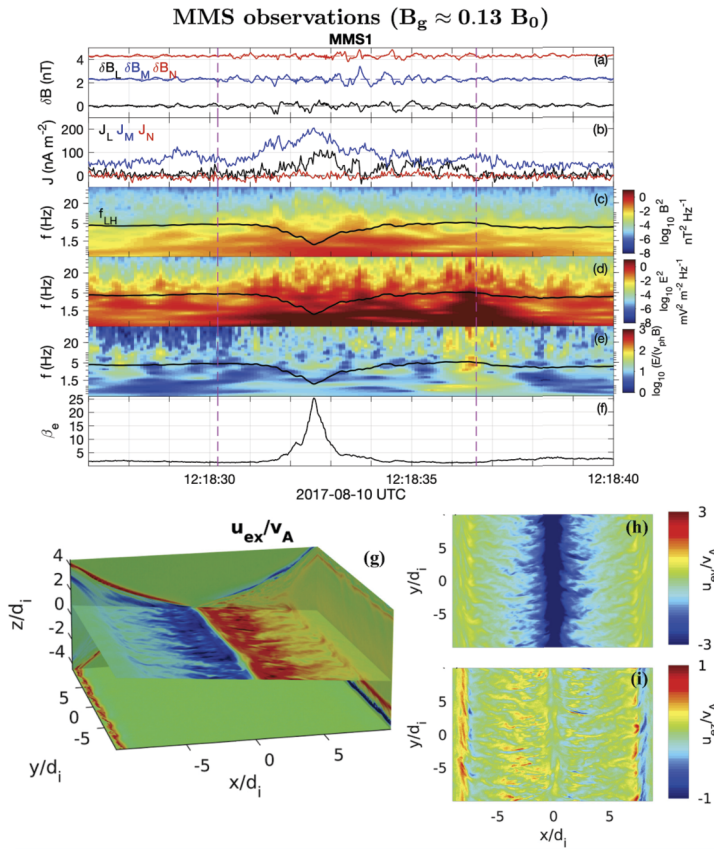


**Fig. 4** *Top*: Electromagnetic lower hybrid scale waves observed by MMS during an EDR crossing in the magnetotail. (a) Three components of magnetic field fluctuations  $\delta \mathbf{B}$ . Offsets of 2.3 nT and 4.3 nT are added to  $\delta B_M$  and  $\delta B_N$ , respectively; (b) current density  $\mathbf{J}$  calculated from particle moments. Spectrum of (c)  $\mathbf{B}$  wave power; (d)  $\mathbf{E}$  wave power; (e)  $\log_{10}(E/(B v_{ph}))$  quantifying the electromagnetic component of the fluctuations. (f)  $\beta_e$ . The black line indicates  $f_{lh}$ . The vertical dashed magenta lines bound the region where the electromagnetic lower hybrid waves are observed. Based on Cozzani et al. (2021). *Bottom*: Electron velocity fluctuations associated with lower hybrid waves near the diffusion region from a 3D PIC simulation of symmetric reconnection with guide field  $B_g = 0.3 B_0$ . (g) 2D slice along the current sheet associated with reconnection. The color shading indicates electron velocities in the x-direction (normal to the current sheet). (h) and (i) the same slices showing electron velocities in the y- and z-directions (out-of-plane and along the reconnecting  $\mathbf{B}$ ), respectively. Adapted from Le et al. (2019)

propagating electromagnetic drift instability (Ji et al. 2004, 2005). The current density fluctuations at approximately the lower hybrid timescale and the broadband feature of the wave fields are comparable to the turbulent electron flow structures of the lower hybrid waves in 3D kinetic simulations (Le et al. 2019) (see Figs. 4g–4i). However, further measurements and 3D simulations are needed to understand the coupling between lower hybrid waves, current sheet instabilities, and the EDR structure.

For zero guide fields, theory and simulations (Daughton 2003) show that the electrostatic short-wavelength mode ( $k\rho_e \sim 1$ ) is confined at the edges of the current sheet, and only the electromagnetic long-wavelength mode ( $k\sqrt{\rho_i\rho_e} \sim 1$ ) is present in the center of the current sheet. In the reconnection context, the zero guide field case has been investigated in

detail in a simulation study (Wang et al. 2021) showing a picture consistent with the results from Daughton (2003), namely that the long-wavelength lower hybrid mode develops at the current sheet center, while the short-wavelength mode develops at the separatrices. However, the short-wavelength wave is found to penetrate towards the midplane, and this could explain the MMS observation of short-wavelength lower hybrid waves close to the current sheet midplane during magnetotail reconnection events with negligible guide fields (Wang et al. 2022b). Wang et al. (2021) also show that while long-wavelength lower hybrid waves lead to oscillations of the current density, vortices do not form in zero guide-field reconnection.

Wang et al. (2022b) investigated lower hybrid waves at MMS magnetotail reconnection diffusion-region crossings characterized by guide field values ranging from 1% to 30% of the upstream magnetic field. The direction of wave propagation and the dominant magnetic field component of the fluctuations vary considerably among the events, although a majority of wave propagation directions lie approximately in the current sheet plane. Both long-wavelength electromagnetic and short-wavelength electrostatic modes are observed in the diffusion regions, including events with negligible guide fields. It was speculated that the short-wavelength mode was excited in separatrix regions and penetrated toward the current sheet mid-plane.

To better understand the generation of the lower hybrid waves in thin electron-scale current layers with a moderate guide field, Ng et al. (2020) performed 2D and 3D PIC simulations of magnetic reconnection with a 30% guide field, mimicking the event reported by Chen et al. (2020). Ng et al. (2020) showed that lower hybrid waves develop immediately downstream of the electron jet reversal in the electron current layer. The lower hybrid waves observed in the 3D simulations propagate along the outflow direction (perpendicular to the ambient magnetic field at the midplane, i.e., the guide field) and affect the flow pattern by creating electron vortices that are similar to in situ observations (Chen et al. 2020). A 3D kinetic simulation of strong guide-field reconnection similarly showed electrostatic waves developing near the EDR and propagating into the outflow region (Ng et al. 2023). These results demonstrate the importance of the guide field, which allows for the short-wavelength,  $k\rho_e \sim 1$ , lower hybrid waves to develop at the reconnection midplane, potentially leading to anomalous resistivity and heating, as shown in a recent laboratory experiment (Yoo et al. 2024). These findings open new possibilities in the context of 3D reconnection. For example, as mentioned by Chen et al. (2020), the new dynamics imposed by the lower hybrid waves in the current layer may lead to secondary tearing at the wave scale.

One of the major advances made with MMS is resolving particle distributions at sufficiently high frequency to reveal wave-particle interactions. Thus, MMS, along with numerical simulations, can resolve detailed information on the wave properties. By assuming that electrons remain close to frozen in and that the waves tend to be localized near boundary layers, the electrons form vortex-like motions, which in turn generates parallel magnetic field fluctuations (Norgren et al. 2012). Evidence of this vortex-like motion has been reported in both symmetric and asymmetric reconnection. In Graham et al. (2019), electron moments resolving electron density and velocity fluctuations associated with the waves were used to investigate the properties of the lower hybrid waves. Figures 5a–5b show an example of lower hybrid waves in the IDR at Earth's magnetopause (Khotyaintsev et al. 2016; Graham et al. 2022), where the electron moments can resolve the fluctuations associated with the waves. Figure 5c shows that the electrons remain approximately frozen in to the magnetic field. Density perturbations are also observed in association with the waves (Fig. 5d). Similarly, Ergun et al. (2017) and Ergun et al. (2019) found density and velocity fluctuations associated with these waves and interpreted them as corrugations of the current sheet.



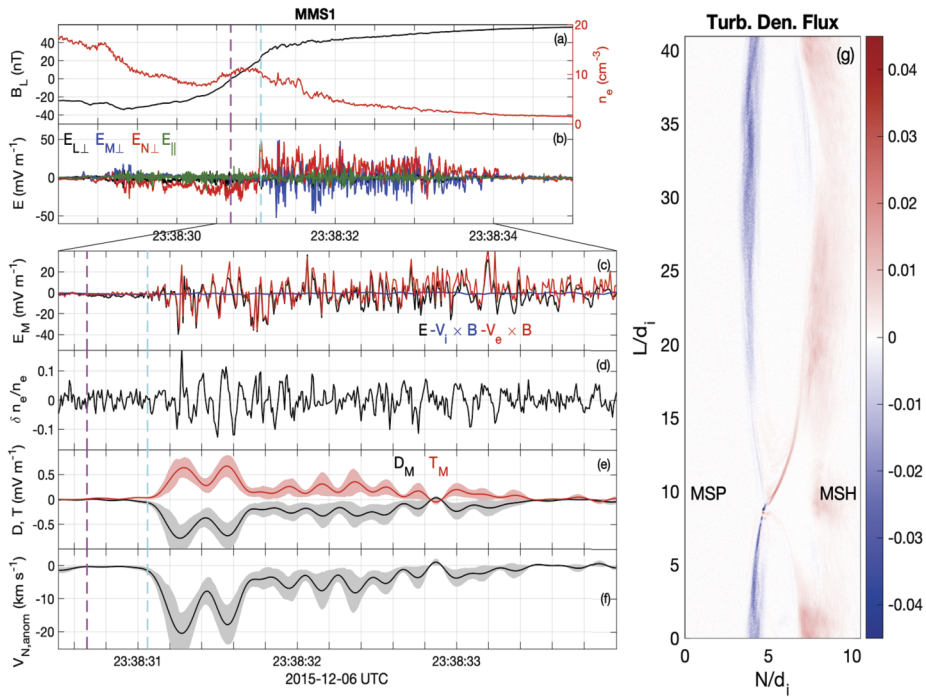


**Fig. 5** Example of lower hybrid waves in the inflow region of magnetic reconnection at Earth's magnetopause, based on Graham et al. (2022). (a) Reconnection magnetic field  $B_L$  (black) and electron number density  $n_e$  (red). (b) Perpendicular and parallel components of the electric field  $\mathbf{E}$ . (c)  $E_M$  (black) and  $\mathbf{M}$  components of  $-\mathbf{V}_i \times \mathbf{B}$  (blue), and  $-\mathbf{V}_e \times \mathbf{B}$  (red). (d) Normalized electron density perturbations  $\delta n_e/n_e$ . (e)  $\mathbf{M}$  components of  $\mathbf{D}$  (black) and  $\mathbf{T}$  (red). (f) Anomalous electron drift in the direction normal to the magnetopause  $V_{N,anom}$ . (g) Anomalous density flux of lower hybrid waves in a three-dimensional asymmetric reconnection simulation. Based on Price et al. (2020)

Lower hybrid waves are a prime candidate for anomalous resistivity, as they generate large electric fields and density perturbations (Fig. 5d). Estimates from spacecraft observations have found that the anomalous resistivity is small (Mozer et al. 2011; Graham et al. 2017a). However, these observations relied on the spacecraft potential to infer density fluctuations, which can be unreliable when large electric fields are present. Recently, Graham et al. (2022) used MMS observations to directly evaluate these anomalous terms for quasi-electrostatic lower hybrid waves at Earth's magnetopause by resolving the fluctuations in the electron moments. This was possible using the highest temporal resolution electron moments (Rager et al. 2018). The study focused on the effects of lower hybrid waves on reconnection, in particular anomalous resistivity and diffusion. The anomalous effects can be evaluated by decomposing quantities into quasi-stationary and fluctuating terms,  $Q = \langle Q \rangle + \delta Q$ , where  $\langle \dots \rangle$  is the ensemble average over space or time and  $\delta Q$  is the fluctuating quantity associated with the waves. This decomposition is then applied to the electron momentum equation

$$m_e \frac{\partial (n_e \mathbf{V}_e)}{\partial t} + m_e \nabla \cdot (n_e \mathbf{V}_e \mathbf{V}_e) + \nabla \cdot \mathbf{P}_e + en_e (\mathbf{E} + \mathbf{V}_e \times \mathbf{B}) = 0, \quad (1)$$

where  $e$ ,  $m_e$ ,  $n_e$ ,  $\mathbf{V}_e$ , and  $\mathbf{P}_e$  are the unit charge, electron mass, electron number density, electron bulk velocity, and electron pressure tensor, respectively. Applying the above decomposition then averaging yields the momentum equation in terms of the stationary quantities and the anomalous terms, which result from the ensemble average of the correlations between fluctuating quantities. After rearranging and neglecting the time derivative, the averaged electric field can be expressed as:

$$\langle \mathbf{E} \rangle + \langle \mathbf{V}_e \rangle \times \langle \mathbf{B} \rangle = -\frac{\nabla \cdot \langle \mathbf{P}_e \rangle}{\langle n_e \rangle e} - \frac{m_e}{\langle n_e \rangle e} \nabla \cdot (\langle n_e \rangle \langle \mathbf{V}_e \rangle \langle \mathbf{V}_e \rangle) + \mathbf{D} + \mathbf{T} + \mathbf{I}, \quad (2)$$

where we have neglected the time derivative and introduced the anomalous terms  $\mathbf{D}$ ,  $\mathbf{T}$ , and  $\mathbf{I}$ . These anomalous terms can be expressed as (Graham et al. 2022)

$$\mathbf{D} = -\frac{\langle \delta n_e \delta \mathbf{E} \rangle}{\langle n_e \rangle}, \quad (3)$$

$$\mathbf{T} = -\frac{\langle n_e \mathbf{V}_e \times \mathbf{B} \rangle}{\langle n_e \rangle} + \langle \mathbf{V}_e \rangle \times \langle \mathbf{B} \rangle, \quad (4)$$

$$\mathbf{I} = -\frac{m_e}{e \langle n_e \rangle} [\nabla \cdot (\langle n_e \mathbf{V}_e \mathbf{V}_e \rangle) - \nabla \cdot (\langle n_e \rangle \langle \mathbf{V}_e \rangle \langle \mathbf{V}_e \rangle)], \quad (5)$$

where the three terms refer to the anomalous resistivity, anomalous momentum transport, and anomalous inertial terms, respectively. In these expressions  $n_e$  and  $\mathbf{V}_e$  are treated as separate quantities, while it is common to treat the electron flux  $n_e \mathbf{V}_e$  as a single quantity (Le et al. 2018).

Graham et al. (2022) found that  $\mathbf{D}$  and  $\mathbf{T}$  can reach amplitudes comparable to the reconnection electric field ( $\sim 1 \text{ mV m}^{-1}$ ) but mostly cancel each other out, while  $\mathbf{I}$  is negligible. The approximate cancellation of  $\mathbf{D}$  and  $\mathbf{T}$  was found to be due to electron fluctuations remaining close to frozen-in [cf., Fig. 5c] (Graham et al. 2019, 2022). As a result, the contribution to the reconnection electric field and reconnection rate is small. Figure 5e shows the out-of-plane components of  $\mathbf{D}$  and  $\mathbf{T}$ , which approximately cancel each other out. Additionally, the waves do not reach the center of the current sheet, so the anomalous terms were found to be negligible there.

The anomalous terms were also evaluated in three-dimensional simulations of magnetopause reconnection (Le et al. 2017, 2018; Price et al. 2016, 2017, 2020; Pritchett 2013). These results showed that either  $\mathbf{D}$ ,  $\mathbf{T}$ , and  $\mathbf{I}$  could provide significant contributions to the reconnection electric field in the diffusion region. The exact contributions depend on the guide-field strength and method of performing the ensemble average (Le et al. 2018). However, a careful examination suggests that the contribution to the anomalous terms mainly results from the large-scale kinking or bending of the current sheet (Le et al. 2018), often with wavelengths on much larger ion scales. Overall, both simulations and observations suggest that the quasi-electrostatic short-wavelength lower hybrid waves do not contribute significantly to the reconnection electric field.

By applying the same procedure to the continuity equation and using Fick's law, an anomalous diffusion coefficient can be defined as

$$D_{\perp} = -\frac{\langle \delta n_e \delta V_{e,N} \rangle}{\nabla \langle n_e \rangle}, \quad (6)$$

where  $\langle \delta n_e \delta V_{e,N} \rangle$  is an anomalous flux in the direction normal to the boundary. An anomalous drift speed in the normal direction can be calculated as  $V_{N,anom} = \langle \delta n_e \delta V_{e,N} \rangle / \langle n_e \rangle$ .



This diffusion coefficient has been calculated from Cluster (Vaivads et al. 2004) and MMS observations (Graham et al. 2022), as well as numerical simulations (Le et al. 2018; Price et al. 2020). From observations, Graham et al. (2022) found that  $D_{\perp}$  was variable at the magnetopause and reached large values of  $\sim 10^9 \text{ m}^2 \text{ s}^{-1}$ , which is sufficient to broaden the magnetopause. Statistically, the largest values of  $D_{\perp}$  tended to occur closer to the EDR rather than along the separatrices. The sign of  $D_{\perp}$  was found to consistently correspond to diffusion from the magnetosheath toward the magnetosphere. Similar electron diffusion was also found in simulations (Le et al. 2018; Price et al. 2020). Although electrons remain close to frozen in, irreversible transport is possible via  $\mathbf{E} \times \mathbf{B}$  trapping, in which the vortical motion of electrons associated with large-amplitude lower hybrid waves becomes strong enough for the electron orbits to become chaotic (Kleva and Drake 1984; Price et al. 2020). The net effect of this diffusion is to broaden the boundary layer and facilitate mixing between magnetosheath and magnetospheric electrons. This mixing has been seen in MMS observations (Wang et al. 2017; Graham et al. 2017a, 2022) and kinetic simulations (Le et al. 2017, 2019). In summary, recent observations and simulations suggest anomalous resistivity due to lower hybrid waves is small and does not likely affect the reconnection rate; however, anomalous diffusion is often sufficiently large to broaden the boundaries where the waves occur.

**Streaming Instabilities and Electrostatic Waves** Near the EDR, strong out-of-plane currents occur. In antiparallel reconnection, these currents are approximately perpendicular to  $\mathbf{B}$ , while for guide-field reconnection these currents become closely aligned with  $\mathbf{B}$ . In addition, the stronger magnetic field due to the guide field at the X line tends to keep electrons magnetized and gyrotopic. The strong currents can become unstable to instabilities, for instance, due to beams, streaming instabilities, and temperature anisotropies. These instabilities can potentially thermalize particle distributions and dissipate the current via wave-particle interactions. Recently, Khotyaintsev et al. (2020) showed that electrostatic Debye-scale waves and turbulence developed in the diffusion region of a guide-field reconnection event at Earth's magnetopause. In the diffusion region, electron distributions composed of a core population and beam were observed. They found that these distributions were unstable to Buneman and beam-mode waves, producing broadband waves with a range of phase speeds. These waves can then thermalize the jet by converting the kinetic energy into thermal energy.

Fully kinetic simulations have been used to investigate streaming instabilities and turbulence in the diffusion region of reconnection. Jara-Almonte et al. (2014) showed using 2D simulations that Debye-scale electrostatic turbulence due to streaming instabilities can develop in the diffusion region for parameters typical of the outer magnetosphere. Specifically, the instabilities developed when there was a significant scale separation between the Debye length and the electron inertial length. Yao et al. (2022a) and Yao et al. (2022b) used the electron distributions from a 3D simulation of reconnection as initial conditions for high-resolution local simulations to study the instability of these distributions. They found that the distributions were unstable to both electrostatic and electromagnetic waves, which propagate both parallel and perpendicular to  $\mathbf{B}$ . Simulations of guide-field reconnection show evidence of the Buneman and beam-driven instabilities in the diffusion region (Che et al. 2010, 2011; Muñoz and Büchner 2018), similar to observations. However, these instabilities occur for strongly magnetized low-beta plasmas. Such parameters are typical of the solar corona but are less common in Earth's magnetosphere. Nevertheless, reconnection with guide fields as strong as the reconnection magnetic field,  $B_g \sim B_0$  can occur, particularly at Earth's magnetopause (Øieroset et al. 2016; Zhou et al. 2018). Similarly, strong-guide-field

$B_g > B_0$  reconnection occurs in Earth's magnetosheath (Wilder et al. 2018), although the plasma beta is typically relatively high  $\beta \sim 1$ .

**Whistler Waves** Electromagnetic whistler waves are frequently observed in and near the EDR of reconnection. Whistlers observed near the EDR have been attributed to electron temperature anisotropy (Khotyaintsev et al. 2016; Cao et al. 2017). However, it remains unclear if field-aligned whistler waves are generated in or near the EDR because whistlers generated in the separatrixes can propagate toward the diffusion region. Recent observations have reported whistlers in the diffusion region at Earth's magnetopause (Zhong et al. 2022). Zhong et al. (2022) found that the local electron distributions were stable to whistler emission and argued that the waves were most likely generated in the separatrixes and propagated toward the X line.

In the case of guide-field reconnection, the strong out-of-plane currents and associated electron beams can generate oblique quasi-electrostatic whistler waves via Landau resonance. Khotyaintsev et al. (2020) found evidence for quasi-electrostatic whistler waves generated by electron beams. A recent study by Wang et al. (2022a) of multiple magnetopause crossings near the EDR of guide-field reconnection found that oblique whistlers were generated locally by electron beams, while parallel propagating whistlers were generated by the temperature anisotropy of the background population. Thus, there are potentially multiple sources of whistler waves near the X line.

### 3.2 Separatrix Regions

The magnetic reconnection separatrixes have been shown to exhibit a variety of plasma wave modes. In symmetric magnetotail reconnection, the separatrixes are typically characterized by fast, cold electron beams propagating toward the X line. For asymmetric reconnection at Earth's magnetopause, the electron distributions in the separatrixes can become more complicated due to magnetospheric and magnetosheath plasmas having distinct densities and temperatures.

**Whistler Waves** Electromagnetic whistler waves have been reported in the separatrixes of both dayside reconnection (Graham et al. 2016b; Le Contel et al. 2016; Wilder et al. 2016) and magnetotail reconnection (Huang et al. 2016; Ren et al. 2019). Field-aligned whistler waves were reported by Graham et al. (2016b) at the magnetopause, who investigated the electron distributions associated with the waves. They found that within the magnetospheric separatrix regions the electron distributions were characterized by an electron beam propagating away from the X line and a loss of energetic magnetospheric electrons propagating away from the X line. Graham et al. (2016b) argued that the loss-cone or temperature anisotropy associated with the partial loss of energetic electrons was the source of the observed whistlers. At the dayside magnetopause, oblique whistler waves associated with electron beams have been found, which coincided with electrostatic solitary waves (ESWs) (Wilder et al. 2016, 2017, 2019). These observations showed the presence of both electron temperature anisotropy ( $T_{e\perp} > T_{e\parallel}$ ) and electron beams at half the electron Alfvén speed, suggesting the presence of competing mechanisms for whistler generation. Wang et al. (2022a) investigated the competition between whistlers driven by beams and electron temperature anisotropy in detail using observations of multiple events. They showed that further away from the X line, whistler waves were more likely to have high ellipticity and a narrow frequency band around half the electron cyclotron frequency. These waves were largely driven by electron anisotropy, with the beams providing additional cyclotron resonance.

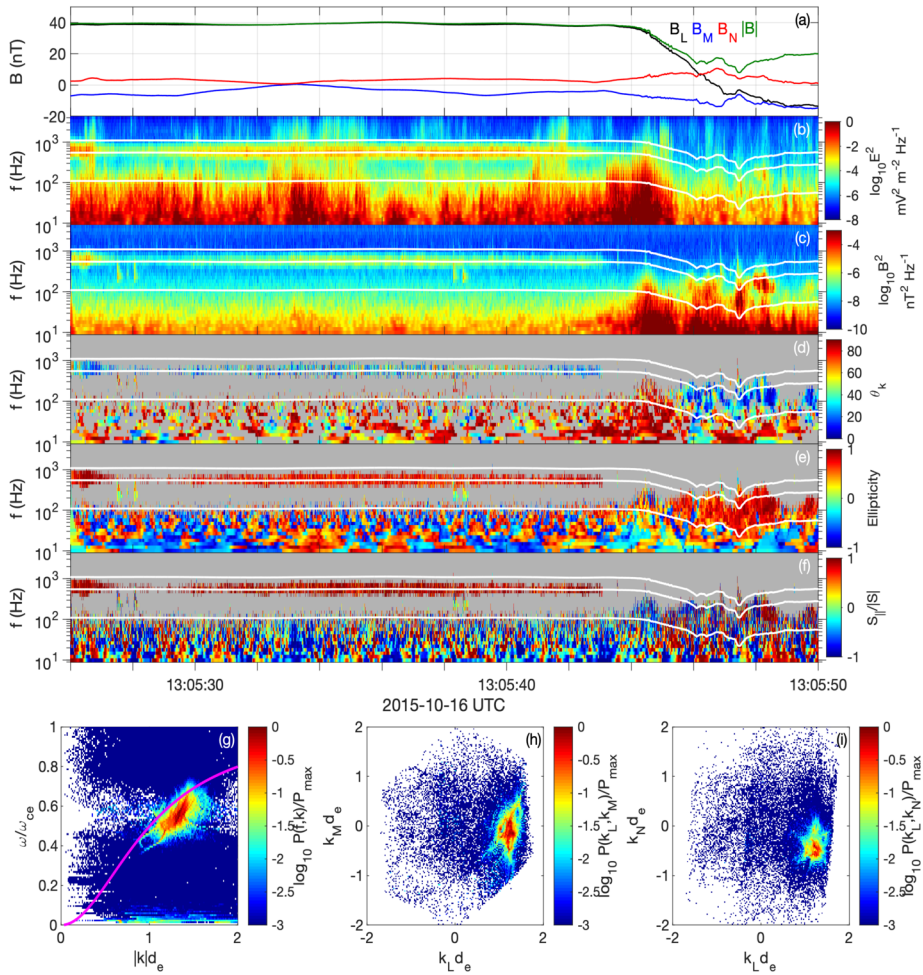


**Fig. 6** Example of whistler waves at the magnetopause based on Le Contel et al. (2016) and Yoo et al. (2018). The whistler waves were observed near the separatrix region of asymmetric reconnection. (a) Magnetic field  $\mathbf{B}$  in boundary normal LMN coordinates. (b) and (c) Frequency-time spectrograms of  $\mathbf{E}$  and  $\mathbf{B}$ . (d)–(e) Spectrograms of wave-normal angle  $\theta_k$ , ellipticity, and ratio of parallel to total Poynting flux  $S_{\parallel}/S$ . Data from MMS1 is used in panels (a)–(e). The white lines in the spectrograms indicate  $0.1f_{ce}$ ,  $0.5f_{ce}$  and  $f_{ce}$ . (g) Frequency-wave number spectrum of whistler waves computed using four-spacecraft phase-differencing between 13:05:26.5 and 13:05:27.0 UT. The magenta line is the whistler dispersion relation predicted by cold plasma theory. (h)–(i) Wave power in the  $k_L$ – $k_M$  and  $k_L$ – $k_N$  planes

Closer to the X line, whistler waves exhibited broadband frequency spectra with varying ellipticity and were more likely to be generated by Landau resonance with the beam. Whistler waves appear to be ubiquitous to magnetic reconnection, and have also been observed during events in the turbulent magnetosheath (Vörös et al. 2019). In guide-field reconnection in the magnetosheath, it was shown that anisotropy-driven whistlers in the separatrix may be damped by parallel electric fields before they reach the EDR (Wilder et al. 2022).

Figure 6 shows an example of whistler waves at Earth's magnetopause observed by MMS1, based on Le Contel et al. (2016) and Yoo et al. (2018). Figure 6a shows  $\mathbf{B}$  in

boundary-normal coordinates. The magnetopause crossing occurs around 13:05:46 UT, where  $\mathbf{B}$  reverses direction. In this event, the whistler waves are observed on the magnetospheric side of the magnetopause. The waves are seen in the spectrograms of  $\mathbf{E}$  and  $\mathbf{B}$  at frequencies near  $0.5f_{ce}$  (Figs. 6b and 6c). The whistler waves are identified using polarization analysis of the electromagnetic fields. Figures 6d–6f show spectrograms of wave-normal angle  $\theta_k$ , ellipticity, and the ratio of parallel to total Poynting flux  $S_{\parallel}/S$ . For these waves  $\theta_k$  tends to vary between  $0^\circ$  and  $\sim 40^\circ$ , meaning the wave propagation varies between field-aligned and oblique. The ellipticity remains close to 1, which is a characteristic signature of whistler waves. Figure 6f shows that  $S_{\parallel}/S$  remains close to 1 corresponding to propagation along  $\mathbf{B}$ , which in this case is toward the reconnection X line (Le Contel et al. 2016). Figures 6g–6i show the dispersion relation for the whistler waves at the beginning of the interval, calculated from the four spacecraft. Such calculations of the dispersion relation are crucial to determining the resonant energies of the electrons.

In the magnetotail, whistler waves have been observed and shown to be associated with fast electron beams (Ren et al. 2019). Ren et al. (2019) argued that whistler waves could be generated via Landau resonance with the inflow electron beam. Similar results were found in kinetic simulations of symmetric reconnection (Fujimoto 2014).

Using a kinetic simulation, Goldman et al. (2014) showed that whistler waves propagating toward the X line can be generated via Cherenkov emission from fast-moving electron holes. These whistlers can propagate into the diffusion region while the electron holes generating them dissipate in the separatrix. Evidence of whistler waves generated via Cherenkov emission was found in Earth's magnetotail using the MMS spacecraft (Steinvall et al. 2019a). However, the whistlers generated by the electron holes were typically found to be damped quickly (Steinvall et al. 2019a), limiting how far they can propagate away from the electron holes generating them.

**Electrostatic Solitary Waves and Electron Phase Space Holes** In addition to electromagnetic waves, nonlinear electrostatic waves and solitary structures are also prominent at the separatrix. In the magnetotail, cold lobe electrons are accelerated towards the X line forming beams, which are unstable to instabilities that can develop ESWs, which in turn can thermalize the electron population (Fujimoto 2014; Egedal et al. 2015; Norgren et al. 2020). When the electrostatic potential associated with the ESWs is positive, they are often interpreted as the manifestation of electron phase space holes. Direct observation of the particle phase-space structure is challenging due to their short observation times. However, recently Mozer et al. (2018) used MMS Fast Plasma Investigation electron data and a superimposed epoch analysis of a group of ESWs to calculate the electron phase-space density and show that the electron distributions were consistent with electron holes. Norgren et al. (2022) used MMS Electron Drift Instrument data to provide continuous time sampling electron fluxes of a group of ESWs in a limited velocity space interval. The changes in electron fluxes were shown to be consistent with predicted electron distributions across electron holes.

Figure 7 shows an example of electron holes observed by MMS at a magnetotail separatrix crossing (Norgren et al. 2020). In Fig. 7a the cold lobe electrons are accelerated parallel to  $\mathbf{B}$ . In this region, strong parallel electric field fluctuations develop (Fig. 7b). The electric fields are characterized by bipolar fluctuations, which are a characteristic signature of electron holes. Using the four MMS spacecraft, the frequency-wave number power spectrum can be calculated (cf., the Appendix) and is shown in Fig. 7d. Most of the electron holes have speeds comparable to, but slightly below, the electron beam speed, consistent with generation by the beam-plasma instability, while some slower electron holes are observed, consistent with generation via the interaction of the electron beam with ions (Norgren et al.

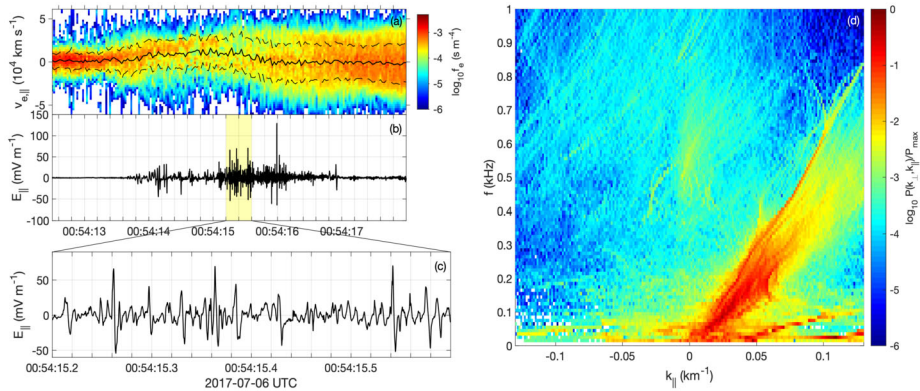


**Fig. 7** Example of electron holes observed in the magnetotail separatrix region, based on Norgren et al. (2020), showing the electron distributions in the separatrix region and the associated electric fields. (a) One-dimensional reduced electron distribution along **B**. The solid black line is the parallel electron bulk speed  $V_{e,||}$  and the dashed lines indicate  $V_{e,||} \pm v_{e,th}$ , where  $v_{e,th}$  is the electron thermal speed. (b) Parallel electric field  $E_{||}$ , showing large-amplitude waves. (c) Zoom in of  $E_{||}$  where the bipolar signatures of electron holes are seen. (d) Power spectrum of  $E_{||}$  as a function of  $k_{||}$  and  $f$  computed from the four-spacecraft phase-difference method (cf., the Appendix)

2015). These observations are consistent with simulations of symmetric reconnection, which show large amplitude ESWs propagating toward the X line (Egedal et al. 2015).

ESWs have also been reported in the separatrices of asymmetric dayside reconnection. For example, Graham et al. (2015) found that ESWs can develop in both the magnetospheric and magnetosheath separatrices. They had positive potentials and were interpreted as electron holes. At the dayside magnetopause separatrix, ESWs with negative potentials associated with the mixing of cold magnetospheric and warm magnetosheath plasma have been observed (Holmes et al. 2018b).

**Ion-Acoustic Waves** Ion-acoustic waves have been found to develop in the separatrix region of magnetopause reconnection (Uchino et al. 2017; Steinvall et al. 2021). They are electrostatic waves with frequencies near the ion plasma frequency  $f_{pi}$  and are typically characterized by magnetic-field-aligned electric fields. For the ion-acoustic instability to grow, it is often necessary that the ions are cold,  $T_i \ll T_e$  (Stringer 1964), which restricts the occurrence of ion-acoustic waves to instances when cold ions are the dominant ion component of one of the reconnecting plasmas. Recent observations by MMS have shown that ion-acoustic waves can develop when cold magnetospheric ions enter the separatrix region, where strong electron-carried currents provide enough free energy to drive the instability (Steinvall et al. 2021). Steinvall et al. (2021) argued that the ion-acoustic instability could lead to current dissipation in the separatrices and cold-ion heating. Similar ion-acoustic waves have also been observed in recent laboratory experiments of magnetic reconnection (Zhang et al. 2023).

Finally, large-amplitude parallel electrostatic waves associated with the mixing of cold magnetospheric and warm magnetosheath plasma have been observed on the magnetospheric side of the dayside magnetopause separatrix (Ergun et al. 2016). These can have amplitudes exceeding  $100 \text{ mV m}^{-1}$ . A topic of future research will be what additional roles these waves play in magnetic reconnection.

**Double Layers** Double layers are localized regions with a net potential change. Double layers are observed in the reconnection separatrices and are associated with the fast electron



flows. In simulations, double layers accelerate electrons along  $\mathbf{B}$  toward the X line to form beams, which are unstable to streaming instabilities and generate ESWs (Fujimoto 2014; Egedal et al. 2015).

Double layers have been observed in the plasma sheet boundary layer in Earth's magnetotail (Ergun et al. 2009; Yuan et al. 2022), although they were not directly linked to reconnection. Wang et al. (2014) found double layers in the separatrix region of reconnection in Earth's magnetotail using Cluster observations. They found that the double layers propagated away from the X line, and might accelerate electrons. Evidence of double layers has been reported in the separatrix regions of magnetopause reconnection in association with electron mixing (Holmes et al. 2019). Overall, the observations of double layers associated with reconnection are rather limited and further observations are needed.

**Lower Hybrid Drift Waves** The presence of lower hybrid and related drift waves has also been reported on the separatrices of magnetic reconnection. Indeed, the largest amplitude lower hybrid waves reported in magnetic reconnection simulations tend to occur along the separatrices. In particular, lower hybrid waves develop along the magnetospheric separatrices of dayside reconnection, where density and ion pressure gradients are strong (Graham et al. 2022). Recent observations show that lower hybrid waves can also develop in the magnetosheath separatrices of asymmetric magnetopause reconnection (Tang et al. 2020a). In addition, lower hybrid waves have been reported in the separatrices of reconnection in the magnetosheath (Vörös et al. 2019), and in the magnetotail (Holmes et al. 2021). Magnetic corrugations associated with drift waves can also extend from the separatrix well into the EDR (Wilder et al. 2019; Ergun et al. 2019), and could be associated with patchy reconnection. Like near the diffusion region, the lower hybrid waves can smooth plasma gradients and facilitate plasma mixing.

**Langmuir and Upper Hybrid Waves** Both Langmuir and UH waves have been observed in or near the separatrices of reconnection at the magnetopause and in the magnetotail. Cluster observations have shown that enhancements in wave power around  $f_{pe}$  occur in the separatrices of high-latitude reconnection at Earth's magnetopause (Khotyaintsev et al. 2004; Retinò et al. 2006). In Earth's magnetotail, UH waves were observed in the separatrices close to the diffusion region (Farrell et al. 2002) and were associated with electron beams (Farrell et al. 2003). Similarly, Viberg et al. (2013) observed plasma frequency waves, interpreted as Langmuir waves, in the outer separatrix regions in association with fast electron beams propagating away from the X line. Graham et al. (2023) investigated the statistical occurrence of Langmuir and UH waves in Earth's magnetotail and showed that Langmuir and UH waves were associated with electron beams. A fraction of these beams were consistent with electrons escaping along newly reconnected field lines in the outer separatrix region.

### 3.3 Ion Outflow

Magnetic reconnection produces non-Maxwellian ion and electron distribution functions that are far from thermal equilibrium. The outflow region of reconnection is particularly rich in non-Maxwellian distributions (Lapenta et al. 2018) leading to the development of kinetic instabilities. The onset of the instabilities produces waves which in turn bring the distribution functions toward isotropization.

**Temperature Anisotropy Instabilities** A common example of ion distribution functions found in the outflow region are anisotropic distributions, either with the parallel temperature larger than the perpendicular  $T_{i,\parallel}/T_{i,\perp} > 1$  or vice versa  $T_{i,\parallel}/T_{i,\perp} < 1$  (the parallel and perpendicular direction of  $T_{i,\parallel}$  and  $T_{i,\perp}$  are based on the direction of the background magnetic field). The ion temperature behavior in the reconnection-related regions has been highlighted by observational and numerical studies (Hietala et al. 2015; Wu et al. 2013). The outflow region, in particular, hosts anisotropic ion distribution functions that could rapidly trigger various instabilities such as the ion firehose (developing if  $T_{i,\parallel}/T_{i,\perp} > 1$ ), mirror, and ion cyclotron instabilities (developing if  $T_{i,\parallel}/T_{i,\perp} < 1$ ) (Gary 1993). As a result, the ion distribution functions are isotropized while low-frequency ion-scale wave modes are generated. This is confirmed by ARTEMIS observations in the deep magnetotail (spacecraft located at  $X \sim -45 R_E$ , (Vörös 2011)) and numerical simulations using different models (Finelli et al. 2021) showing that the ion population in the magnetic reconnection outflow regions is shaped by the anisotropy-driven instabilities. ARTEMIS observations in Earthward and tailward reconnection exhausts also showed compressional waves in correspondence with regions unstable to the ion cyclotron, mirror, and firehose instability (Wang et al. 2020). Furthermore, the development of the temperature anisotropy depends on the location with respect to the X line. Wu et al. (2013) used THEMIS observations at different locations along the magnetotail to show that  $T_{i,\perp}/T_{i,\parallel}$  is enhanced in correspondence of bursty bulk flows (BBFs). Also, the spread of the ion distribution in the  $T_{i,\perp}/T_{i,\parallel}$  versus  $\beta_{i,\parallel}$  parameter space is reduced closer to Earth ( $\beta_{i,\parallel} = 2\mu_0 n_i T_{i,\parallel}/B^2$ , where  $\mu_0$  is the vacuum magnetic permeability and  $n_i$  is the proton number density).

A large body of work exists about these instabilities constraining ion anisotropy in the solar wind (Gary et al. 1976; Hellinger et al. 2006; Bale et al. 2009; Matteini et al. 2013a). Among these studies, Matteini et al. (2013b) investigated the relationship between the temperature anisotropy-driven instabilities and the onset of reconnection by simulating temperature anisotropic plasma mimicking the solar wind. However, the interplay between reconnection and the ion firehose, mirror and cyclotron instability is still relatively unexplored, especially in near-Earth plasmas. Few recent efforts have been made to investigate the effect of these instabilities on magnetosheath ions using MMS observations (Maruca et al. 2018). Recently, Richard et al. (2023) investigated the anisotropic distributions in the ion outflow regions of magnetotail reconnection. They showed that the observed ion anisotropies could lead to instability, although the effects of the resulting wave-particle interactions were too slow to return the distributions to isotropy. Rather, chaotic and quasi-chaotic motion of the ions in the current sheet was found to more quickly return ion distributions to isotropy.

**Ion Firehose Instability** The ion firehose instability is a kinetic instability which is driven by temperature anisotropy  $T_{i,\parallel}/T_{i,\perp} > 1$  (Gary et al. 1998; Hellinger and Matsumoto 2000). The instability may arise in plasma with sufficiently high temperature anisotropy  $T_{i,\parallel}/T_{i,\perp}$  and ion  $\beta_{i,\parallel}$ . The ion firehose instability has two branches: a low-frequency ( $f < f_{ci}$ ) whistler firehose branch that propagates parallel to the background magnetic field (Gary et al. 1998) and a non-propagating oblique branch, called the Alfvén firehose branch by Hellinger and Matsumoto (2000). The non-propagating ion firehose branch has a linear growth rate comparable to or even higher than the propagating branch. The presence of the ion firehose instability in the ion outflow has been identified by Hietala et al. (2015). Their work presented ARTEMIS spacecraft observations in the magnetotail and PIC simulations showing that the ion firehose threshold is greatly exceeded within patchy regions in the reconnection outflow. Their results show that the driving of the temperature anisotropy by reconnection is stronger and faster than the linear growth of the instability, so the waves cannot efficiently remove

the temperature anisotropy. This behavior is explained by ongoing magnetic reconnection constantly refilling the outflow region with unstable plasma. However, as highlighted by Wu et al. (2013), the ion temperature anisotropy highly depends on the location in the outflow with respect to the X line.

Large-scale simulations of reconnection have shown that the current becomes unstable far downstream of the X line, resulting in current sheet disruption and current filamentations forming (Lottermoser et al. 1998; Karimabadi et al. 1999; Arzner and Scholer 2001; Liu et al. 2012; Higashimori and Hoshino 2015). These simulations found that the ion firehose threshold can be satisfied in the outflow region. Using fluid theory, Arzner and Scholer (2001) argued that the instability was similar to the ion firehose instability due to counter-streaming ions, although velocity shears can also contribute to the instability. These results underline the complex interplay between magnetic reconnection and instabilities.

**Ion Mirror Instability** The interaction between magnetic reconnection and ion mirror instability is still quite unexplored. Laitinen et al. (2010) presented Cluster observations of strong mirror modes in the magnetosheath and strongly time- and space-varying reconnection jets at the magnetopause. Since the timescales of both phenomena were similar (of the order of one minute), these results suggest that mirror mode fluctuations in the magnetosheath can affect magnetopause reconnection, either by imposing modulation of continuous reconnection or by triggering bursts of reconnection. This scenario has been confirmed in hybrid-Vlasov global magnetospheric simulations (Hoilijoki et al. 2017). Hau et al. (2020) provided evidence of the presence of mirror mode waves – identified by observing the anticorrelation between the magnetic field and the density signals – in the vicinity of magnetic reconnection sites at the magnetopause. The two analysed MMS events were located in the magnetosphere dawn flank and the characteristic length associated with the mirror waves was smaller in these events than the size that is typically observed in the outer magnetosheath, at larger distances from the magnetopause. Despite the relatively limited amount of observational studies reporting mirror waves associated with reconnection, theoretical studies suggest that the mirror instability could significantly affect the reconnection process. Chiou and Hau (2003) predict a mixed mirror-tearing instability scenario where the mirror instability could increase the tearing instability growth rate. However, it is important to note that this study investigated the resistive tearing-mode instability. More recently, Winarto and Kunz (2022) investigated the relationship between reconnection and ion mirror instability in a magnetized, collisionless, high-beta plasma using hybrid-PIC simulations. They showed that initially, the mirror modes modify the current sheet by reducing its thickness, and then tearing modes with wavelengths comparable to the mirror mode become unstable, triggering reconnection on smaller scales and at earlier times with respect to the case of the current sheet not perturbed by mirror modes.

**Electron Firehose Instability** The presence of electron temperature anisotropy  $T_{e,\parallel}/T_{e,\perp} > 1$  can provide free energy for the development of the electron firehose instability (Hollweg and Völk 1970). There are two distinct electron firehose wave modes. One electron firehose branch is characterized by parallel propagation with respect to the background magnetic field; the other is non-propagating, and it is predicted to develop for oblique wave-normal angles (Gary and Nishimura 2003). It is now established that the non-propagating mode has a lower threshold and a larger growth rate than the propagating mode. As with its ion counterpart, the electron firehose instability has been investigated quite extensively in the solar wind context (Verscharen et al. 2022, and references therein) since it is invoked as one of the sources of isotropization to explain the quasi-isotropic electron distributions observed in the solar wind.



A few efforts have been devoted to investigating the electron firehose instability in magnetospheric plasmas. Notably, a Cluster statistical study of electron distributions in the magnetosheath shows that the electron distribution function is constrained by the electron firehose instability threshold (Gary et al. 2005). Similar conclusions are presented in a statistical observational study focusing on dipolarization fronts (DFs) in the magnetotail (Zhang et al. 2018). Using MMS, Graham et al. (2021) found near the magnetopause and in the magnetosheath that the parallel temperature anisotropy was constrained by the electron firehose instability threshold, with  $T_{e,\parallel}/T_{e,\perp}$  rarely exceeding the threshold. Yet, the role of the electron firehose anisotropy in constraining the temperature anisotropy in the regions associated with reconnection is still largely unknown. Recently, electron firehose fluctuations have been identified in the reconnection outflow in 3D PIC simulations (Le et al. 2019) and in Earth's magnetotail using in situ MMS observations (Cozzani et al. 2023) (see Fig. 8). Figure 8 shows a comparison of electron firehose observations and the associated temperature anisotropies (Cozzani et al. 2023) and a 3D kinetic simulation (Le et al. 2019). In both these cases  $T_{e,\parallel}/T_{e,\perp}$  was constrained by the firehose threshold and the observed wave properties were consistent with the oblique electron firehose mode.

**Electron Two-Stream Instability** The electron two-stream instability (ETSI) is another significant source of isotropization of electron distribution functions in the reconnection outflow region. The development of the ETSI has been reported in the EDR (Jara-Almonte et al. 2014) and at the separatrix (Hesse et al. 2018) in symmetric magnetic reconnection simulation without a guide field and in situ observation of the separatrix region in the magnetotail (Norgren et al. 2020). In these cases, the instability was triggered by the presence of counterstreaming electron beams originating in the two inflow regions and interacting in the EDR or by the mixing of inflow and outflow populations at the thin separatrix boundary (see Sect. 3.2). However, ETSI can develop for asymmetric magnetic reconnection as well. Magnetic reconnection at the magnetopause naturally involves the mixing of multiple electron populations of magnetosheath and magnetospheric origin and typically the guide field is non-zero. Tang et al. (2020b) presented an MMS exhaust crossing during magnetopause reconnection where MMS measures high-frequency electrostatic waves generated by the ETSI in the outflow region. They show unstable electron distributions, which are rapidly isotropized, suggesting that wave-particle interaction is important for electron dynamics in the outflow. Figure 9 shows an example of the electrostatic waves and the associated electron distribution. The electron distribution consisted of a core and a beam, and a fit to the observed distribution yielded linear growth of ETSI.

**Kinetic Alfvén Waves** Alfvén waves are low-frequency, typically electromagnetic waves that are ubiquitous in magnetized plasmas. Shear Alfvén waves are essentially an MHD wave mode. However, if the perpendicular wavelength  $\lambda_{\perp}$  (with respect to the background magnetic field direction) is comparable to kinetic characteristic spatial scales such as the ion gyroradius  $\rho_i$ , kinetic effects become significant and the shear Alfvén waves transition to the Dispersive Alfvén Wave (DAW) modes. In particular, Kinetic Alfvén Waves (KAWs) correspond to the DAW mode that arises in the intermediate-high  $\beta$  regime (Stasiewicz et al. 2000; Chen et al. 2021). KAWs are characterized by  $\lambda_{\perp}\rho_i \sim 1$  and electric fields parallel to the background magnetic field  $E_{\parallel}$  sustained by the electron pressure gradient. The parallel electric fields could have a significant role in enabling particle acceleration and plasma heating. Identification of KAWs is usually based on the transverse spatial scale, which is expected to be comparable to or smaller than the ion gyroradius, and on the ratio between the electric field and magnetic field, which is expected to be close to or larger

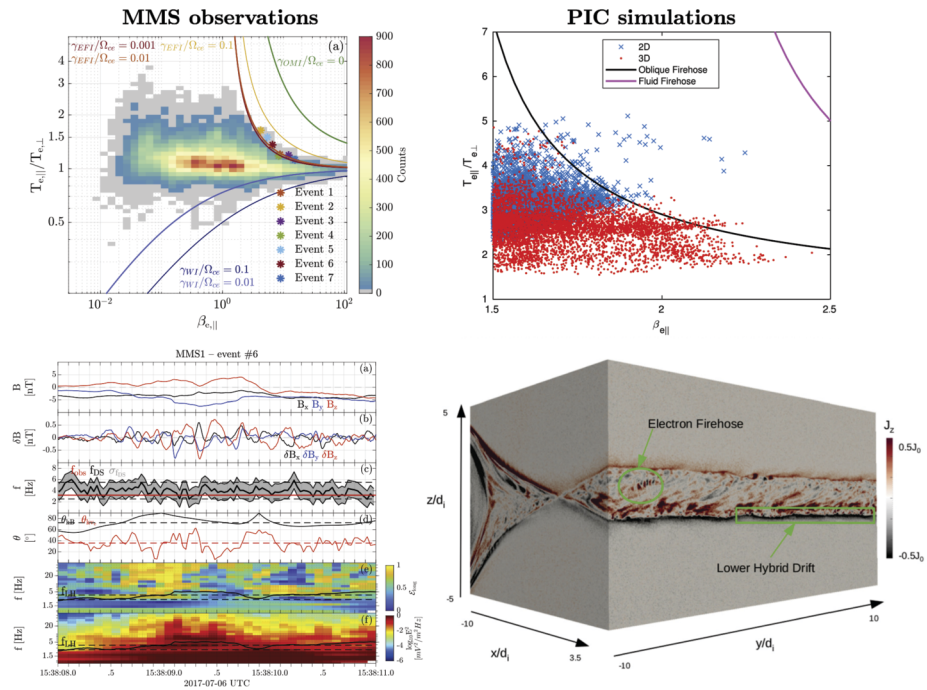


**Fig. 8** Electron firehose waves in the reconnection outflows as observed by MMS (left column panels, adapted from Cozzani et al. 2023) and in 3D PIC simulations (right column panels, adapted from Le et al. 2019). *Top left:* (a) Electron distribution in the parameter space  $\beta_{e\parallel} - T_{e\parallel}/T_{e\perp}$ . The electron population is bounded by the Weibel ordinary-mode instability (OMI) marginal condition of stability (Ibscher et al. 2012). *Bottom left:* Time series of quantities used to identify the non-propagating electron firehose fluctuations. (a) Magnetic field; (b) Magnetic field fluctuations; (c) Observed frequency  $f_{obs}$  (red solid line), Doppler-shift frequency  $f_{DS}$  (solid black line) and associated variability range (grey shaded region) with value  $\sigma_{f_{DS}}$ . (d) Angle between the wave vector direction and background magnetic field direction  $\theta_{kB}$  and angle between the wave vector direction and electron velocity direction  $\theta_{kv_e}$ . (e) Spectrogram of  $\mathcal{E}_{long} = |\mathbf{E} \cdot \hat{\mathbf{k}}|^2 / |\mathbf{E}|^2$ . (f) Spectrogram of the electric field power. The black line is the lower hybrid frequency  $f_{LH}$ , and the dashed black lines indicate the frequency range of the observed fluctuations ( $\Delta f = [2.6, 3.8]$  Hz for this event). *Top right:* distribution in the parameter space  $\beta_{e\parallel} - T_{e\parallel}/T_{e\perp}$ . The magenta curve is the fluid firehose condition  $F_e = \mu_0(P_{e\parallel} - P_{e\perp})/B^2 = 1$  and the black curve is the non-propagating electron firehose instability threshold (same as the red curve in the top left panel). The points are taken in the reconnection outflow. Several points of the 2D run lie well above the electron firehose stability threshold, indicating that the firehose instability acts to regulate the electron temperature anisotropy and it is more efficient in doing so in 3D systems. *Bottom right:* Surface plots of the current density  $J_z$ . Electron firehose fluctuations are present in the outflow region, while lower hybrid drift modes develop at the separatrices. The electron firehose mode develops in a large number of flux tubes scattered throughout the exhaust at different times depending on the local plasma conditions

than the Alfvén speed. A critical property of KAWs is that they can transport energy over large distances in the form of Poynting flux  $\mathbf{S} = \delta \mathbf{E} \times \delta \mathbf{B} / \mu_0$  directed mainly along the ambient magnetic field (see Fig. 10), where  $\delta \mathbf{E}$  and  $\delta \mathbf{B}$  are the wave electric and magnetic fields. For this reason, they are considered a fundamental process contributing to the mutual magnetosphere-ionosphere coupling, to ion energization and heating, and to electron acceleration via parallel electric fields.

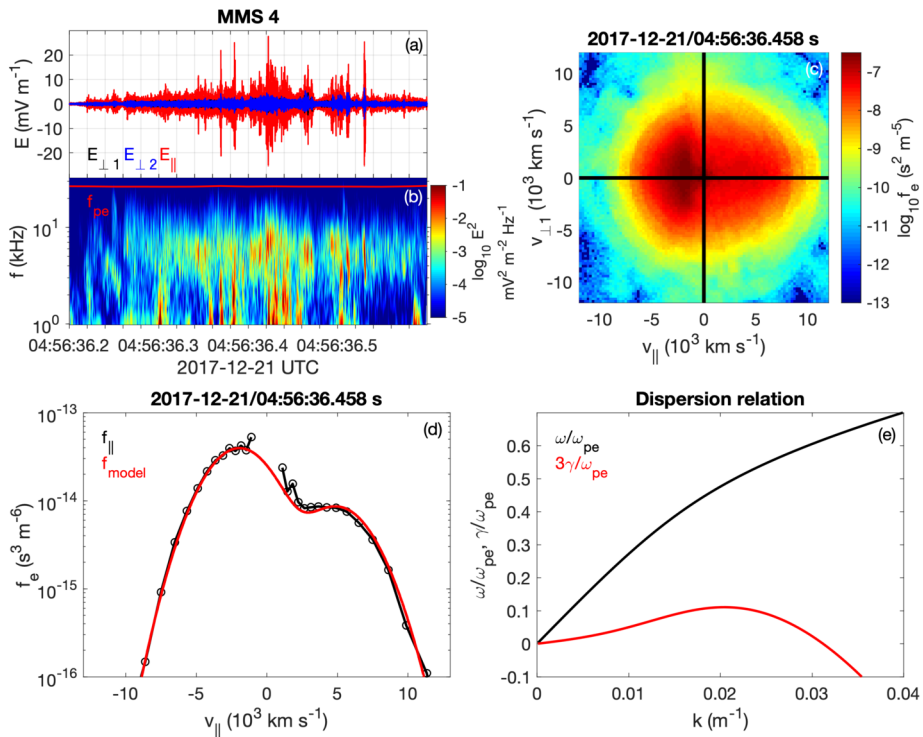


**Fig. 9** Electrostatic wave associated with ETSI in the reconnection outflow of dayside magnetic reconnection observed by MMS4. Based on Tang et al. (2020b). (a) High-frequency  $E$  fluctuations in field-aligned coordinates. (b) Spectrogram of  $E$ . (c) Two-dimensional reduced electron distribution at the time the waves are observed. (d) One-dimensional cut of the electron distribution parallel and antiparallel to  $\mathbf{B}$  (black) and a two-Maxwellian fit to the data (red). (e) Dispersion relation (black) and growth rate (red) predicted from the fitted distribution

KAWs are intimately related to magnetic reconnection as they are proposed to be associated with the Hall reconnection signatures. In particular, Rogers et al. (2001) suggested that the formation of an open outflow typical of fast magnetic reconnection is associated with the generation of whistler waves and KAWs. Also, Dai (2009) presented an approach in which the Hall fields and currents are incorporated in the Alfvén eigenmode theory. Dai (2009) showed that magnetic and electric fields measured in situ across the IDR (Mozier et al. 2002) can be explained in terms of eigenmode theory as they agree with the  $n = 1$  Alfvén eigenmode signatures. KAWs are thought to set the magnetic and electric field Hall structure of the IDR and then propagate away from the reconnection site. Observational evidence of the coexistence of KAWs and magnetic reconnection was presented in several studies (Chaston et al. 2005, 2009; Dai et al. 2011). In particular, Dai et al. (2011) reported observations of KAWs in the magnetotail reconnection outflow region, while Chaston et al. (2009) presented in situ Cluster observations of KAWs in the IDR and in the outflow region of magnetic reconnection. In Chaston et al. (2009) the wave fronts are observed to propagate away from the X line, and the propagation is compatible with KAWs being emitted from a localized source. While the generation mechanism of the KAWs could not be established, this study provides evidence of the presence of KAWs in the exhaust and indicates the X line as the possible generation region. A statistical study by Chaston et al. (2012) considered THEMIS

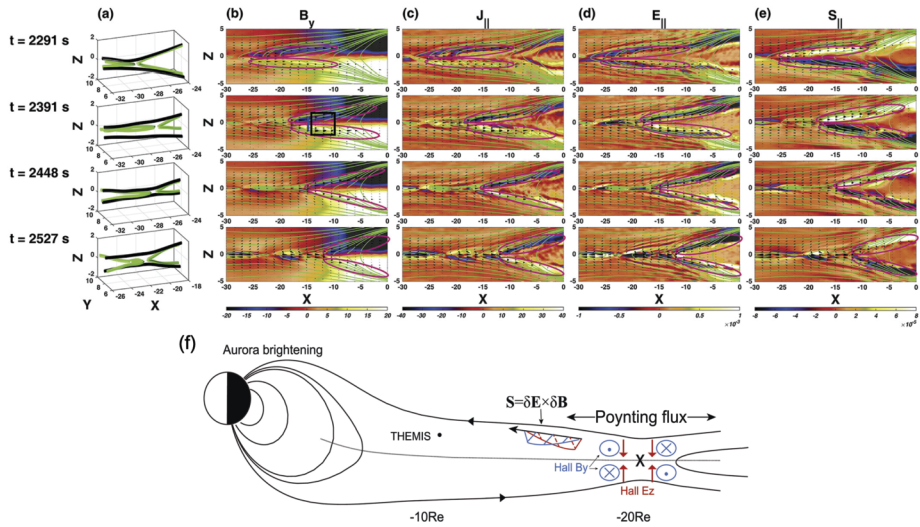


**Fig. 10** Kinetic Alfvén Waves associated with magnetotail reconnection. Signatures of KAWs observed in a global 3D hybrid simulation of Earth's magnetosphere, adapted from Cheng et al. (2020) (panels a–e) and a schematic of the magnetic and electric field Hall patterns associated with KAW and magnetic reconnection in the magnetotail, adapted from Duan et al. (2016) (panel f). Time evolution of (a) magnetic field lines at the X line; (b) contours of  $B_y$  (GSE); (c) contours of the current density parallel to the background magnetic field  $J_{\parallel}$ ; (d) contours of the electric field parallel to the background magnetic field  $E_{\parallel}$ ; (e) contours of the Poynting flux parallel to the background magnetic field  $S_{\parallel}$ . The axis  $X$ ,  $Y$  and  $Z$  are in units of Earth's radius  $R_E$ . The pink ovals show the time evolution of the same wave structure generated by reconnection and its Earthward propagation. (f) Schematic depicting the Earth's magnetotail, the Hall magnetic and electric field structure associated with KAWs at the reconnection site and the KAWs parallel Poynting flux transporting energy towards Earth and likely accounting for aurora brightening

observations of fast flows in Earth's magnetotail and showed that low-frequency electromagnetic waves consistent with KAWs are continuously radiated outward toward the lobe. The fact that KAWs are generated in the IDR and then propagate in the outflow region is further supported by simulation studies (Shay et al. 2011; Liang et al. 2016; Huang et al. 2018; Cheng et al. 2020). A similar conclusion has been drawn from reconnection observed in a laboratory experiment featuring mutually attracting flux ropes in a linear mirror device (Shi et al. 2019). KAWs were identified, and the temporal variation of the KAW's amplitude was correlated with the temporal variation of the reconnection rate, supporting the relationship between the two.

As mentioned above, KAWs are thought to play a primary role in magnetospheric-ionospheric coupling. Notably, the Poynting flux carried by KAWs has been proposed as a possible source for aurora (Angelopoulos et al. 2002; Wygant et al. 2002; Shay et al. 2011), connecting magnetotail and magnetopause reconnection to ionospheric processes. In particular, since KAWs can transport energy at super-Alfvénic velocities, they could account for the observed early onset of aurora with respect to the Alfvénic transit time from the reconnection site (Angelopoulos et al. 2008). Duan et al. (2016) reported THEMIS observations in the near-Earth plasma sheet showing signatures of KAWs during the substorm expansion phase. The KAWs were observed in correspondence with dipolarization, likely due to intermittent reconnection. Several observational studies reporting intense KAWs in correspondence with high-speed flows suggest that the observed waves carry sufficient Poynting flux flowing Earthward that they could account for auroral brightening at low altitudes (Stawarz

et al. 2017; Chaston et al. 2012; Angelopoulos et al. 2002). Simulation studies have provided evidence supporting this scenario. Shay et al. (2011) estimated that KAW energy is able to propagate to Earth's ionosphere and create aurora, and similar conclusions were drawn in a simulation study quantifying the attenuation of the Hall quadrupolar magnetic field structure propagation as a KAW during magnetic reconnection (Sharma Pyakurel et al. 2018). These estimations are valuable but constrained by the limited size of the simulation domains. Recently, Gurram et al. (2021) suggested that the main carrier of wave energy away from the reconnection site in magnetotail reconnection was shear Alfvén waves (SAWs) instead of KAWs. By performing fully-kinetic simulations with high mass ratio ( $m_i/m_e = 400$ ) and open boundary conditions, Gurram et al. (2021) found that both KAWs and SAWs are generated and that the damping rate of KAWs is enhanced so that the SAWs are the main wave energy carrier. The wave energy transported by the SAWs is higher by an order of magnitude with respect to previous estimates and could account for the energy deposited in the ionosphere and lead to the aurora. In summary, despite the significant progress in the investigation of KAWs, namely their relation to reconnection and the KAW-related energy transport, more work is needed to fully understand their role in terms of magnetosphere-ionosphere coupling.

High-cadence in situ measurements by MMS enables KAWs to be investigated with an unprecedented level of detail. Zhang et al. (2017) presented MMS observations at the magnetopause confirming that the electric and magnetic field Hall pattern was observed as far as  $40 d_i$  away from the reconnection site, and it is consistent with the KAW mode. The high cadence of MMS particle measurements combined with small inter-spacecraft separation allowed for the calculation of spatial gradients at kinetic scales, enabling the detailed study of wave-particle interactions. Gershman et al. (2017) reported nonlinear wave-particle interactions between electrons and KAWs in the reconnection outflow region at the magnetopause. The trapped population of electrons may contribute to the saturation and damping of the KAWs. Nonlinear wave-particle interactions such as nonlinear Landau damping and stochastic heating play a key role also in the acceleration and heating of ions, as shown in 3D hybrid simulations investigating KAWs associated with magnetic reconnection (Liang et al. 2017). Recently, the set of MMS data presented by Gershman et al. (2017) was analyzed to accurately determine the KAWs perpendicular wavelength  $\lambda_\perp$  by using a particle-sounding technique that can only be applied to high-resolution particle instruments. As the required time resolution is higher than one-fifth of the wave period, only MMS observations can be used in this case (Liu et al. 2023). Liu et al. (2023) showed that  $\lambda_\perp/\rho_{th,i} \approx 2.4 \pm 0.7$ , where  $\rho_{th,i} = \sqrt{2m_p T_{i,\perp}/eB_0}$  is the proton thermal gyro-radius ( $m_p$  is the proton mass,  $T_{i,\perp}$  is the ion temperature perpendicular to the ambient magnetic field  $B_0$ ). While confirming the ion-scale nature of KAWs, this result imposes a limit to the energy exchange between KAWs and ions. Indeed, the highest perpendicular energy  $W_{\perp,m}$  that can be gained by ions via coherent wave-particle interaction is related to the perpendicular wavelength  $\sqrt{2m_p W_{\perp,m}/eB_0} \lesssim \lambda_\perp \approx (2.4^2) \rho_{th,i} \approx 5.76 \rho_{th,i}$ .

Apart from the generation in the IDR, several other KAW generation mechanisms have been proposed. KAWs could be generated by mode conversion (Hasegawa and Chen 1976), which is particularly relevant in regions with a significant gradient in Alfvén speed, such as the magnetopause (Shi et al. 2013). Velocity shears could also facilitate the generation of KAWs (Taroyan and Erdélyi 2002; Nykyri et al. 2021). KAWs could also be generated by intermittent reconnection (Cao et al. 2013). Also, KAWs have been proposed as a key constituent of the turbulent reconnection outflows. Huang et al. (2012) show that the dispersion relation computed in the turbulent outflow of magnetic reconnection in the Earth's magnetotail agrees with the Alfvén-whistler wave mode.



### 3.4 Jet Fronts

Jet fronts are regions where the outflow jets from magnetic reconnection interact with the ambient plasma sheet of the magnetotail. The jet fronts are often ion scale boundaries characterized by sharp increases in the normal to the current sheet component of  $\mathbf{B}$ . In the case of the Earth's magnetotail, this can be interpreted as the field configuration getting closer to a dipole field, and therefore the fronts are often called dipolarization fronts (DFs). There is also a decrease in density as the outflow plasma has a lower density than the plasma sheet. The thickness of the jet front boundaries is typically comparable to the ion kinetic scales, and thus the plasma gradients can be unstable to the generation of various waves. For example, drift waves and interchange instabilities can develop at the fronts, while whistler waves and streaming instabilities develop behind the fronts.

**Lower Hybrid Waves** Lower hybrid drift waves are among the most commonly observed waves associated with dipolarization fronts. The gradients in  $\mathbf{B}$  and thermal pressure, and the associated cross-field currents, provide the source of instability, similar to the magnetopause. Cluster and THEMIS observations have shown lower hybrid waves developing at dipolarization fronts (Zhou et al. 2009a; Greco et al. 2017; Khotyaintsev et al. 2011; Divin et al. 2015b). Zhou et al. (2009a) found lower hybrid waves in regions of enhanced Hall electric field and suggested that diamagnetic drifts were responsible for the waves. Similarly, Divin et al. (2015b) found that the waves were consistent with generation by the lower hybrid drift instability by comparing Cluster observations with linear kinetic theory (Yoon and Lui 2008). Based on observations, the lower hybrid waves have been proposed to contribute to both ion (Greco et al. 2017) and electron heating (Khotyaintsev et al. 2011).

Recently, the properties of lower hybrid waves have been investigated using MMS. Le Contel et al. (2017) investigated the properties of lower hybrid waves and suggested the waves contribute to electron heating. Pan et al. (2018) investigated a dipolarization front with electron-scale structures across the front. These structures were consistent with a rippling structure along the front due to lower hybrid waves. Figure 11 shows the rippled dipolarization front observed by MMS in Pan et al. (2018). Figure 11a shows the profile of  $\mathbf{B}$  in boundary-normal coordinates. The rippling results in large  $\mathbf{J}$  in the normal direction and large fluctuating  $\mathbf{E}_\perp$  (both the normal and in-plane components). The electric fields are dominated by the Hall electric field, with a minor contribution from the electron pressure divergence. A simple model of the front ripples assuming pressure balance shows good agreement with the observations (Figs. 11e–11g). Statistical investigation of lower hybrid waves at dipolarization fronts by Hosner et al. (2022) concluded that the waves are a consistent feature of the fronts.

Simulations of magnetotail reconnection show that as reconnection proceeds, the region near the X line is filled with the upstream low-density plasmas, and thus, the density and pressure gradients become smaller than those occurring during reconnection onset in simulations. This can stabilize plasma instabilities, such as LHDI, near the X line (Nakamura et al. 2016). Instead, at this later stage of reconnection, the sharpest gradients develop at the jet fronts, leading to LHDI waves developing there (Vapirev et al. 2013; Lapenta et al. 2014; Divin et al. 2015a; Nakamura et al. 2016). Similarly, simulations show that velocity shear instabilities at DFs can excite waves in the lower hybrid frequency range (Lin et al. 2019). Simulations have also shown that the gradients in the jet front region can also induce the ballooning/interchange instability (BICI), which breaks up the front into ion-scale finger-like structures (Nakamura et al. 2002; TanDokoro and Fujimoto 2005; Guzdar et al. 2010; Lapenta and Bettarini 2011; Pritchett 2015b). 3D kinetic simulations of reconnection

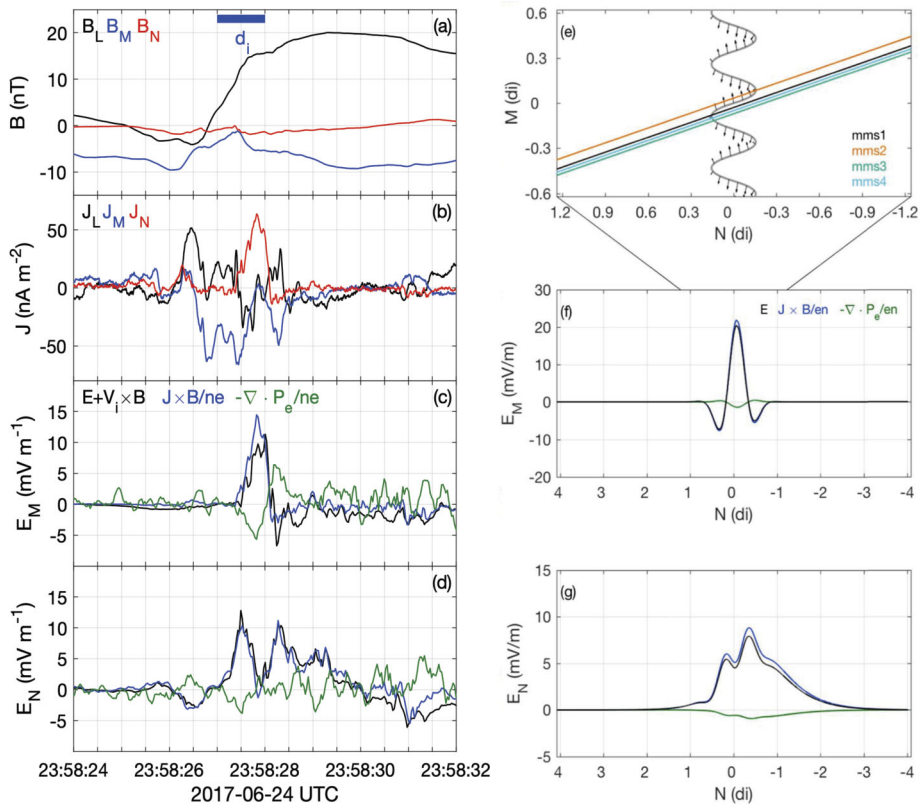


**Fig. 11** A rippled dipolarization front observed by MMS in Earth's magnetotail, adapted from Pan et al. (2018). Panels (a)–(d) present MMS observations of the DF, while panels (e)–(g) show a model of the rippled DF. (a)  $\mathbf{B}$ , (b) current density  $\mathbf{J}$  calculated using the Curlometer technique. (c) and (d) Normal  $\mathbf{N}$  and out-of-plane  $\mathbf{M}$  components of  $\mathbf{E} + \mathbf{V}_i \times \mathbf{B}$  (black),  $\mathbf{J} \times \mathbf{B}/ne$  (blue), and  $-\nabla \cdot \mathbf{P}_e/ne$  (green). (e) Model of the perturbed DF where the arrows indicate the direction of  $\mathbf{E}$ . The colored lines indicate the trajectory of MMS across the DF. (f) and (g) Model predictions of the components of  $\mathbf{E}$  in the  $\mathbf{M}$  and  $\mathbf{N}$  directions, respectively

showed that LHDI at jet fronts could nonlinearly couple with the BICI, leading to additional growth of BICI finger-like structures (Nakamura et al. 2016). The nonlinear evolution of LHDI at the front dissipates magnetic energy and diffuses the compressed front layer (Nakamura et al. 2019).

**Whistler Waves** Pileup of the reconnected magnetic flux (increase of  $\mathbf{B}$ ) behind the front drives the electron VDF to perpendicular anisotropy  $T_{e\perp} > T_{e\parallel}$  due to conservation of magnetic moment  $\mu = m_e v_{e\perp}^2 / 2B$ , known as the betatron effect (Birn et al. 2022). Such anisotropic VDFs eventually become unstable to the generation of field-aligned whistlers due to whistler temperature anisotropy instability (Kennel and Petschek 1966). Generation of whistlers in the flux-pileup region (FPR) behind the front has been observed in numerical simulations (Fujimoto and Sydora 2008) and spacecraft observations (Le Contel et al. 2009; Khotyaintsev et al. 2011). It has been statistically confirmed that whistler generation is a characteristic feature of the FPR, with about half of the observed fronts having associated whistler emission (Viberg et al. 2014; Li et al. 2015). The waves are in cyclotron resonance

with suprathermal ( $>1$  keV) electrons, and these electrons with large pitch angles provide the major contribution to the wave growth (Grigorenko et al. 2023). Adiabatic betatron heating is thus followed by the wave generation, which in turn leads to pitch-angle scattering of the resonant electrons reshaping the distribution function (Artemyev et al. 2022), making the overall heating process non-adiabatic. The scattering process is relatively fast: for the magnetotail conditions, the characteristic scale is of the order of one second (Khotyaintsev et al. 2011), and thus, the whistler growth effectively regulates the temperature anisotropy driven by the flux pileup, which has been confirmed statistically (Zhang et al. 2018). The whistlers can also scatter energetic electrons into the loss cone, leading to their precipitation (Tsai et al. 2022). As the generated whistlers will propagate out of the generation region (FPR), they will carry away energy in the form of Poynting flux, corresponding to several percent of the suprathermal electron flux (Khotyaintsev et al. 2011; Zhang et al. 2019). The common occurrence of whistlers at the reconnection jet fronts provides smoking-gun evidence of the active pileup of magnetic flux. Therefore, observation of whistlers in combination with other data can be used to identify such a region in cases where only very limited or no particle data is available, e.g., for observations at Jupiter, Ganymede, Saturn, and other planets.

**Electrostatic Waves** The complex ion and electron velocity distributions behind the jet front can also drive electrostatic waves, such as electrostatic solitary waves, broadband electrostatic waves, or electron cyclotron waves. In particular, loss-cone and ring-type electron distributions behind the dipolarization front can excite electrostatic electron cyclotron harmonics (ECHs) (Zhou et al. 2009a). Zhou et al. (2009a) attributed these ECHs to the positive slope in the electron perpendicular velocity distribution function. They suggested that these ECHs could accelerate non-resonant electrons through a stochastic mechanism (Farrell et al. 2003). In addition, Fermi-accelerated parallel electron beams (e.g. Fu et al. 2013) may also drive broadband electrostatic waves with frequencies up to several times the electron cyclotron frequency  $f_{ce}$  (Hwang et al. 2011, 2014). Hwang et al. (2014) found that the Fermi-accelerated electron beams in the flux tube behind the dipolarization front drive two electrostatic wave modes. The low frequency ( $\sim 0.43 f_{ce}$ ) mode was an oblique ( $\theta_{kb} \approx 35^\circ$ ) whistler mode and the high frequency ( $\sim 3.4 f_{ce}$ ) mode was a parallel ( $\theta_{kb} = 0.7^\circ$ ) electron beam mode. The authors speculated that the former could be responsible for ion heating. Fermi-accelerated ion beam VDFs originating from the pre-existing plasma sheet ahead of the front (Eastwood et al. 2015), and cold ions accelerated across the separatrices (Wygant et al. 2005) can also drive ESWs (Liu et al. 2019; Zhang et al. 2022). Liu et al. (2019) suggested that intense electrostatic solitary waves observed behind the DF are generated by an ion-beam instability driven by the fast cold ion beam. Alternatively, Zhang et al. (2022) suggested that ESWs behind the jet fronts are driven by a drift between the hot ion population in the outflow and the cold ion beam originating from the inner magnetosphere. Lakhina et al. (2021) proposed a mechanism for the generation of these ESW in terms of slow and fast ion-acoustic solitons. Using a multi-fluid description with a hot Maxwellian electron core and two ion beams, Lakhina et al. (2021) found two fast and two slow ion-acoustic modes propagating parallel and antiparallel to the background magnetic field. They found that the predicted ion-acoustic solitons are in good agreement with MMS's observations. Liu et al. (2019) suggested that these ESWs can eventually thermalize the unstable ion beams, heating the ions in the reconnection jet.

## 4 Large-Scale Waves

In the previous sections, we primarily focused on kinetic-scale microinstabilities. However, larger-scale macroinstabilities associated with current sheets develop and can have important



consequences for ongoing reconnection and reconnection onset. We briefly describe current sheet kinking and the tearing mode instabilities. The relation between the Kelvin-Helmholtz instability and reconnection is discussed in Stawarz et al. (2024, this collection).

#### 4.1 Flapping and Kinking of Current Sheets

Flapping motions are large-scale ( $\lambda \sim 1 R_E$ ) North-South oscillations of the magnetotail current sheet (Speiser and Ness 1967; Lui et al. 1978). In particular, Gao et al. (2018) distinguished two types of flapping motions: the steady flapping, which consists of a global North-South motion of the current sheet, and the sinusoidal wave-like sheet motion (Speiser 1973). From an observational point of view, the flapping motions are seen as large amplitude oscillations of the Earthward/tailward magnetic field with multiple current sheet crossings (Figs. 12a and 12b). The typical period of these oscillations ranges from  $\sim 10$  minutes (Sergeev et al. 2004) to  $\sim 10$  seconds (Wei et al. 2019). Multi-spacecraft missions, such as Cluster and MMS, enable the type of flapping motion as well as the propagation velocity to be calculated using multi-spacecraft timing (Vogt et al. 2011). The timing method has been used statistically by Runov et al. (2005) to show that the wave-like flapping motion propagates toward the flank of the magnetosphere along the electric current direction (Fig. 12c). Three-dimensional fully kinetic simulations with open boundaries showed that wave-like flapping motions propagate in the duskward direction with a speed close to the Alfvén speed (Sitnov et al. 2014). The measured propagation velocity of the wave-like flapping motions ranges from  $\sim 10 \text{ km s}^{-1}$  to  $\sim 100 \text{ km s}^{-1}$  (Sergeev et al. 2004; Runov et al. 2005).

Various mechanisms have been proposed to excite flapping motions. For instance, Gao et al. (2018) suggested that the steady flapping in the midnight region induces the wave-like flankward propagating flapping motion observed in the flanks. Using MMS, Wang et al. (2019) suggested that solar wind directional change creates a North-South motion of the magnetotail current sheet, which triggers the flapping motions. MMS observed the modulation of the reconnection electric field with the same period as the flapping motions, suggesting that unsteady reconnection may induce the flapping motion (Wei et al. 2019). On the

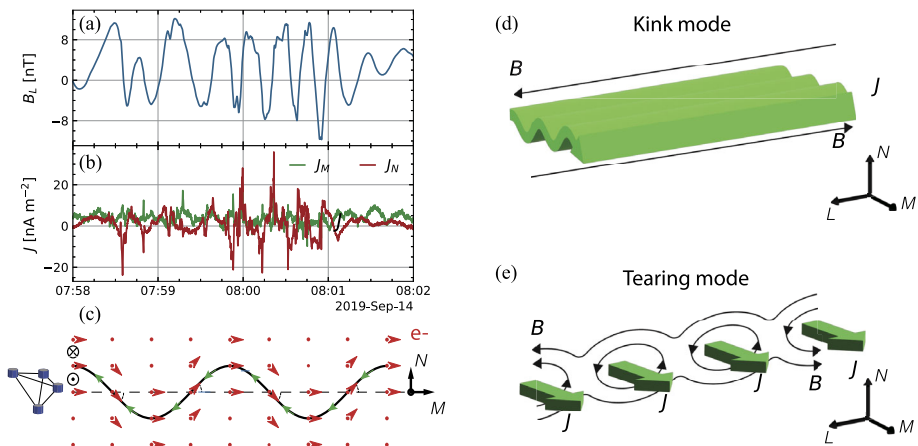


**Fig. 12** Illustrations of flapping and tearing modes associated with large-scale current sheets. Panels (a)–(c) present MMS observation of current sheet flapping. Based on Richard et al. (2021). (a) Magnetic field, (b) current density, and (c) schematic of the drift-kink instability-driven current sheet flapping in the ion frame, showing the electron motion (red) and current direction (green). (d) and (e) Illustrations of the kink mode associated with current sheet flapping and the tearing mode

other hand, linear stability analyses have suggested that the wave-like flapping may result from the MHD double gradient instability (Erkaev et al. 2007), the ion-ion kink instability (Karimabadi et al. 2003; Sitnov et al. 2004), and the drift-kink instability (Daughton 1999). In particular, Karimabadi et al. (2003) found that the wave properties observed by Runov et al. (2003) are in very good agreement with the prediction of the ion-ion kink mode. Recently, Richard et al. (2021) found that the wavelength of the wave-like flapping motion is consistent with the prediction of the drift-kink instability, suggesting that this instability can be responsible for the flapping motion.

## 4.2 Tearing Mode

The tearing mode is particularly interesting because it can generate the conditions required for reconnection onset. The instability develops in current sheets to perturb the magnetic field, potentially leading to the development of X lines and magnetic islands (as illustrated in Fig. 12e). The tearing mode exists in the resistive and collisionless regimes. The resistive tearing mode can be described by the MHD equations in the presence of finite resistivity in the center of the current sheet (Furth et al. 1963). The theory was then extended to collisionless plasma (Coppi et al. 1966) and to plasmas with variable collisionality (Drake and Lee 1977). At Earth's magnetopause and magnetotail, plasmas are essentially collisionless, so other effects must take the place of collisions, such as Landau damping.

Much of the theoretical work has focused on Earth's magnetotail. There, due to the contribution of Earth's dipole magnetic field, the magnetic field configuration has a small but finite component ( $B_z/B_0 \sim 0.1$ ) normal to the current sheet. Therefore, the current sheet is often modeled using a 2D isotropic locally Harris equilibrium (Schindler 1972; Lembedge and Pellat 1982). Due to the finite normal component, the electrons remain magnetized, suppressing the electron Landau dissipation and thus the electron tearing mode (Galeev and Zelenyi 1976). Assuming the electron damping is unimportant for  $T_i/T_e \gg 1$ , Schindler (1974) showed that ion Landau dissipation of unmagnetized ions drives an ion tearing instability. However, for many conditions, the growth rate is too low to be important (Sitnov et al. 2019). Additionally, Lembedge and Pellat (1982) found that ion tearing is prevented by an electrostatic potential due to the electron density compression associated with the tearing mode. Sitnov and Schindler (2010) showed that the stability criteria may be exceeded in the case of a localized magnetic flux accumulation called a  $B_z$  hump. The stability of the non-Harris thin current sheets supported by non-Maxwellian ion VDFs is still debated (Burkhart et al. 1992; Zelenyi et al. 2008).

Kinetic simulations have been used to study the development of tearing instability. The stability of the configuration proposed by Sitnov and Schindler (2010) was tested in multiple two-dimensional PIC simulations (Sitnov et al. 2013; Bessho and Bhattacharjee 2014; Pritchett 2015a). While all studies revealed the development of an instability leading to reconnection, the nature of the driving instability is debated. In particular, Bessho and Bhattacharjee (2014) showed the development of an electron tearing mode for a sufficiently small normal magnetic field. Simulations have generally found growth of an electron tearing mode, where the electron physics drives the instability. Imposing an external driving electric field along the out-of-plane direction compresses the current sheet and reduces the normal field, leading to electron demagnetization and electron tearing (Hesse and Schindler 2001; Liu et al. 2014; Pritchett 2005).

Currently, there is limited observational evidence of tearing mode in space plasmas. A small number of studies have investigated tearing modes within Earth's magnetosphere. For example, Bakrania et al. (2022) used machine learning techniques to identify signatures in electron distributions consistent with tearing modes in Earth's magnetotail. Lu et al.

(2020) argued that a magnetotail reconnection onset event was consistent with electron tearing occurring, while the ion tearing mode was found to be unlikely. Similarly, Genestreti et al. (2023) investigated reconnection onset in the magnetotail and found that onset was consistent with the electron tearing instability. At present, it is unclear to what degree the tearing mode can account for the onset of reconnection in Earth's magnetopause and magnetotail. Some observations have found evidence of the tearing mode in the solar wind (Réville et al. 2020). Analyses of tearing mode remain largely theoretical, and direct observations are currently limited. Further observational work is needed to determine the role of tearing modes in the onset of reconnection.

## 5 Discussion

The review in Sect. 3 shows that we now understand well the types of waves that can develop in reconnection regions. High-resolution fields measurements from spacecraft enable the types of waves associated with reconnection to be identified and characterized. Spacecraft such as Cluster and MMS have enabled waves to be characterized using multi-spacecraft methods. Similarly, multi-spacecraft methods enable the region where waves develop in relation to reconnection to be identified. Additionally, the observation of background particle distributions and estimates of plasma gradients and electric currents enable the instabilities responsible for the waves to be identified. Similar analyses from kinetic simulations and laboratory experiments enable the location of the waves in relation to reconnection to be identified and the underlying instabilities to be investigated. Thus, the type of waves that develop in different regions, their properties, and the underlying instabilities are generally well understood.

A crucial ongoing question is what effect these waves have on the plasma and how these waves affect reconnection. Generally, the effect of waves will be to return unstable plasmas to stability. Most of the knowledge of the effects of waves on plasmas is based on theoretical work or numerical simulations. Numerical simulations enable wave-particle interactions to be isolated from other plasma processes. Using in situ observations to study the effects of waves on the plasma is generally very difficult. For lower frequency waves up to lower-hybrid frequency, MMS has resolved the fluctuations in the particle distributions and moments associated with the waves (Gershman et al. 2017; Graham et al. 2022). This enables wave-particle interactions to be directly investigated. Additionally, wave-particle interactions for waves at higher frequencies, such as whistlers (Kitamura et al. 2022) and electron holes (Mozer et al. 2018; Norgren et al. 2022), have been investigated. These studies suggest further work can be done to quantify the effects of wave-particle interactions on magnetic reconnection and plasmas more generally with current instrumentation. In particular, further work is needed to determine if higher-frequency waves can contribute to anomalous resistivity and electron diffusion near the EDR.

Another ongoing question is the importance of three-dimensional effects when studying magnetic reconnection. Most simulations and observations have modeled or interpreted reconnection in two dimensions, assuming a uniform out-of-plane direction. Recent simulations and observations of reconnection have focused on three-dimensional effects. One of the primary effects when simulating reconnection in three dimensions is that drift waves in the out-of-plane direction develop. Drift waves can develop close to the X line, resulting in significant perturbations in and around the EDR (Cozzani et al. 2021). Three-dimensional simulations and observations have shown that lower hybrid waves tend to broaden the separatrix regions from electron-scale boundaries to hybrid or ion scale boundaries. In addition,

significantly enhanced electron mixing and heating occur in three-dimensional simulations compared with two-dimensional simulations for asymmetric magnetopause reconnection (Le et al. 2017). The cause of the heating due to lower hybrid waves or the associated electron mixing is not fully understood. It has been argued that electron heating can result from Landau damping of lower hybrid waves (Cairns and McMillan 2005; Ren et al. 2022). Observations have shown that these waves have small but finite parallel wave numbers (Graham et al. 2019) so Landau damping of electrons is plausible. Further work is required to determine if the energy transferred to electrons by the waves is sufficient to account for the strong parallel electron heating reported in reconnection observations and simulations.

The recent observations of UH waves in and near the EDR and Langmuir waves in the reconnection separatrixes suggest that these regions are possible sources of electron heating, scattering, and diffusion. These processes could modify reconnection at electron scales (Dokgo et al. 2020a). Due to the challenges in modeling these waves in simulations of magnetic reconnection and the current difficulty in directly quantifying these effects with spacecraft observations, further work is needed to determine the role of these waves in reconnection. These observations also suggest that diffusion regions and separatrixes may be sources of escaping electromagnetic O- or X-mode waves, which could be observed remotely. Langmuir and UH waves can be converted to O- and X-mode waves near the plasma frequency and its harmonics via linear and nonlinear processes. Recent simulations show that UH waves generated by electron distributions can undergo three-wave decay and coalescence to generate electromagnetic waves at  $2f_{pe}$  (Dokgo et al. 2019). Similar results were found for Langmuir and UH waves/electron Bernstein waves by Yao et al. (2022a). However, these simulations used local homogeneous conditions with initial distribution functions based on distributions from observations or simulations of magnetic reconnection. Large-scale three-dimensional kinetic simulations of reconnection, which can resolve Langmuir and UH waves, and the generated electromagnetic waves are not currently feasible. Although electromagnetic waves produced in reconnection regions have been reported on the Sun (Cairns et al. 2018), escaping electromagnetic waves have not yet been reported from in situ observations of magnetic reconnection. Further work is required to better understand magnetic reconnection as a source of escaping electromagnetic waves.

Finally, one of the major ongoing questions is reconnection onset, namely, how is reconnection initiated in thin current sheets and what role do waves and wave-particle interactions play? Tearing modes are often invoked to explain the development of X lines and reconnection onset. However, observational evidence of the tearing mode from spacecraft observations is limited, especially at Earth's magnetopause and in the magnetotail. Identifying signatures of tearing instability in spacecraft observations has proved very challenging and requires further investigation.

## 6 Conclusion

The role waves play in collisionless magnetic reconnection has been studied extensively using spacecraft observations, numerical simulations, and laboratory experiments. Kinetic plasma waves have been found in the reconnection diffusion region, separatrixes, ion outflow regions, and at jet fronts. Significant progress has been made in characterizing the waves developing in these different regions. High-resolution electromagnetic field measurements have enabled the waves to be identified and their properties characterized. Single- and multi-spacecraft observations have been used to determine where these waves occur in relation to magnetic reconnection. Detailed analyses of the particle distribution functions have

been used to determine the source of instability generating the waves. As a result, the type of waves that develop and why they occur in relation to magnetic reconnection are generally well understood. Recent major results are that MMS observations have demonstrated for the first time that the agyrotropic electron distributions produced by the EDR are unstable to large-amplitude electrostatic waves, which had not been previously found in simulations. Additionally, the type of instabilities that cause the observed waves have been identified by comparing the wave properties with the observed particle distribution functions. Significant progress has been made in understanding the role of anomalous resistivity in reconnection due to short-wavelength lower hybrid waves, enabled by the direct measurement of fluctuating electron distributions associated with the waves. Observations and simulations have shown that the effects on the reconnection electric field are small, but anomalous diffusion and plasma mixing due to lower hybrid waves can significantly broaden the boundary layer near the diffusion region and separatrices.

## Appendix: Wave Measurement Techniques

In this section, we summarize important wave analysis techniques, which have been employed to study plasma associated with magnetic reconnection.

### A.1 Multi-Spacecraft Interferometry

Multi-spacecraft methods are most appropriate for waves on scales larger than the probe-to-probe distance and close to the spacecraft separation. Given a collection of spacecraft with known separations, the standard approach assumes a plane-wave structure and uses cross-correlation of fields measurements and the resulting time-delays to determine the phase velocity of the wave (Götz Paschmann 1998). For a matrix of vector separations  $\mathbf{r}$  between spacecraft indexed  $\alpha$  and  $\beta$ , and a corresponding matrix of timings  $t_{\alpha\beta}$ , the basic equation to solve is given by:

$$\mathbf{r}_{\alpha\beta} \cdot \frac{\hat{\mathbf{n}}}{v_{ph}} = t_{\alpha\beta}. \quad (\text{A1})$$

Where  $\hat{\mathbf{n}}$  is the normal vector in the direction of the plane wave. The system can then be solved for  $\hat{\mathbf{n}}/v_{ph}$  using a least squares fitting or other linear algebra technique. In the special case of a tetrahedron, keeping  $\alpha$  fixed, there are three baselines, and the system can be solved exactly by inverting  $\mathbf{r}_{\alpha\beta}$ . The differences in applying this method come from changing how  $t_{\alpha\beta}$  are determined, and how the matrix equation is solved.

The most basic approach of cross-correlating  $E_{\parallel}$  measurements has been used effectively for solitary waves, which have an isolated pulse signature (Tong et al. 2018; Holmes et al. 2018b,a; Steinvall et al. 2019b; Mozer et al. 2018; Lotekar et al. 2020; Kamaletdinov et al. 2021; Norgren et al. 2022). However, it has also been used for wave packets of lower-hybrid, Buneman, and beam-mode waves (Holmes et al. 2021), and whistler waves (Hull et al. 2020; Zhong et al. 2022).

One can extend the above method to the spectral domain by determining a phase difference (and therefore a time delay from  $\Delta t_{\alpha\beta} = \Delta\phi_{\alpha\beta}/\omega$ ). Averaging over a sliding time window, one can compute the complex-valued cross-spectral density  $C(t, \omega)$  as a Fourier transform of the cross-correlation. The phase difference is given by:

$$\Delta\phi = \tan^{-1}(\Im[C(t, \omega)]/\Re[C(t, \omega)]), \quad (\text{A2})$$

where  $\Re$  and  $\Im$  denote the real and imaginary components of  $C(t, \omega)$ . Because  $t$ ,  $\omega$  and  $k$  are directly mapped to one another via the phase velocity and  $\mathbf{r}_{\alpha\beta}$ , the average power spectrum  $P(t, \omega)$  of the fields can be remapped as a function  $P(\mathbf{k}, \omega)$ . Furthermore, from the full wave-vector  $\mathbf{k}$ , spectra in terms of the components  $k_{\parallel}$  and  $k_{\perp}$  can also be compared with theoretical dispersion relations. This method has recently been applied using wavelet rather than Fourier transforms for lower hybrid waves (Graham et al. 2019), whistlers (Zhong et al. 2022), and electron holes (Norgren et al. 2020).

Finally, the k-filtering or wave-telescope technique (see e.g. Capon 1969; Pincon and Lefeuvre 1991; Motschmann et al. 1996; Tjulin et al. 2005) solves the general matrix equation (A3):

$$P(\mathbf{k}, \omega) = \text{Tr} \left[ \left( \mathbf{H}^{\dagger}(\mathbf{k}) \mathbf{M}^{-1}(\omega) \mathbf{H}(\mathbf{k}) \right)^{-1} \right], \quad (\text{A3})$$

where  $\mathbf{M}$  is a large matrix of the time-windowed cross-spectral density of the input vector fields and the spacecraft positions, and  $\mathbf{H}$  is a “shape function” which is typically a matrix of plane waves describing how waves travel between each spacecraft position.  $\mathbf{H}$  could also be chosen to account for three-dimensional structure such as spherical waves or current-sheet shapes. This approach can be further extended by applying various types of adaptive filters or constrained optimization schemes (Narita et al. 2022). The wave-telescope technique plus various extensions has been recently used to identify spectra of mirror mode waves (Narita et al. 2016), kinetic Alfvén waves (Gershman et al. 2018), whistler waves (Yoo et al. 2018), and turbulence in the solar wind from density fluctuations (Roberts et al. 2017).

## A.2 Multi-Probe Interferometry

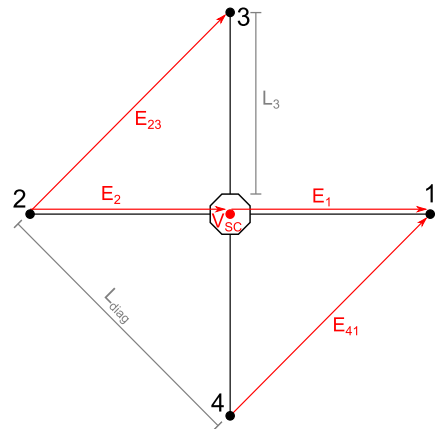
For MMS and many other spacecraft, electric fields are measured using the double probe technique, where the difference in potentials between two probes is used to estimate the component of the electric field between the probes. The probes measure the potential difference  $V_i$  between the probe and the spacecraft, given by  $V_i = V_{p,i} - V_{SC}$ , where  $V_{p,i}$  is the probe potential,  $V_{SC}$  is the spacecraft potential, and the subscript  $i$  refers to the probe number. The probes are typically biased with a current so their potentials remain close to the plasma potential. The electric field is then given by

$$E_{ij} = -\frac{V_j - V_i}{L_{ij}}, \quad (\text{A4})$$

where  $L_{ij}$  is the distance between probes  $i$  and  $j$ . Nominally, the difference is taken from probes on opposite sides of the spacecraft to construct  $E_{ij}$ . Each MMS spacecraft consists of six probes, whence the three-dimensional electric field is constructed. Figure A1 shows the probe configuration in the spin plane; the two axial probes (probes 5 and 6) are out of and into the page. In practice, the conducting spacecraft and booms typically lead to a reduction in  $E_{ij}$  due to local short-circuiting. Therefore, an effective baseline is used for  $L_{ij}$  rather than the physical probe separation (Pedersen et al. 2008).

The fact that the probes are separated in space means that it is possible to use  $V_j$  as multi-point measurements, namely multi-probe interferometry. Multi-probe interferometry has been used to estimate the phase speed or velocities by either comparing different  $V_i$  directly or reconstructing electric fields from different probe combinations. The time delays  $\Delta t$  (Vasko et al. 2018) or the phase differences (Graham et al. 2016a) between measurements are used to estimate the phase speed. Three different methods have been employed:

**Fig. A1** Schematic of the MMS probe configuration in the spacecraft spin plane. The axial probes are into and out of the page



1. The time delays between opposing probe-to-spacecraft potentials to estimate the phase speeds along the probe displacement. For MMS time delays between  $V_1$  and  $-V_2$ ,  $V_3$  and  $-V_4$ , and  $V_5$  and  $-V_6$ . The phase speed and wave vector are calculated using (Vasko et al. 2018):

$$v_{ph} = \left( \frac{\Delta t_{12}^2}{L_1^2} + \frac{\Delta t_{34}^2}{L_3^2} + \frac{\Delta t_{56}^2}{L_5^2} \right)^{-1/2}, k_{ji} = \frac{v_{ph} \Delta t_{ij}}{L_i}, \quad (\text{A5})$$

where  $\Delta t_{ij}$  is the time delay between probes  $i$  and  $j$ ,  $L_j$  is the probe to spacecraft separation and  $k_{ji}$  is the wave number along the  $ji$  direction. The advantage of this method is that it can in theory provide a three-dimensional wave vector when using the three probe pairs. The disadvantage is that  $V_j$  is used, which means that any changes in  $V_{SC}$  due to density fluctuations or electric fields affect the results. At high frequencies, one measurement has a  $\delta V_{SC}$  contribution while the other has a  $-\delta V_{SC}$  contribution, where  $\delta V_{SC}$  refers to fluctuations in the spacecraft potential.

2. The second method involves constructing two spatially separated electric fields in the same direction. For an electric field along the direction of the 12 probe pair this is achieved using (Khotyaintsev et al. 2011; Graham et al. 2015):

$$E_1 = \frac{V_{SC} - V_1}{L_1}, E_2 = \frac{V_2 - V_{SC}}{L_2}, V_{SC} = \frac{V_3 + V_4}{2}. \quad (\text{A6})$$

The fields are aligned and correspond to a spatial separation of  $L_1$ , as illustrated in Fig. A1. Since the method relies on differences between  $V_i$ , the contributions from  $\delta V_{SC}$  should be negligible compared with method 1. However, this method requires the direction of  $\mathbf{k}$  to be known from other methods or needs to be assumed, and is typically only reliable for electrostatic waves with  $\mathbf{k}$  closely aligned with one of the probe pairs, which corresponds to the longest baseline and most reliable estimate of  $V_{SC}$ .

3. The third method involves constructing an electric field from adjacent probes around the spacecraft rather than opposing pairs (Vaivads et al. 2004). The fields  $E_{41} \parallel E_{23}$  (illustrated in Fig. A1) and  $E_{13} \parallel E_{42}$  using equation (A4) and  $L_{diag} = \sqrt{2}L_i$  is used as the baseline. Two time delays can be calculated  $\Delta t_{41,23}$  and  $\Delta t_{42,13}$  to calculate  $v_{ph}$  and  $\mathbf{k}$  in



the spacecraft spin plane (Steinvall et al. 2022):

$$v_{ph} = \left( \frac{\Delta t_{41,23}^2}{L_{diag}^2} + \frac{\Delta t_{42,13}^2}{L_{diag}^2} \right)^{-1/2}, \mathbf{k} = \begin{pmatrix} \frac{1}{\sqrt{2}} & -\frac{1}{\sqrt{2}} \\ \frac{1}{\sqrt{2}} & \frac{1}{\sqrt{2}} \end{pmatrix} \begin{pmatrix} \Delta t_{42,13} \\ \Delta t_{41,23} \end{pmatrix} \frac{v_{ph}}{L_{diag}}. \quad (A7)$$

This method provides  $v_{ph}$  and  $\mathbf{k}$  in the spin plane, but this method cannot be applied to the axial probes. Like method (2) the effects of  $\delta V_{SC}$  should be small.

We note that performing multi-probe interferometry is generally difficult and can be prone to error. In particular, in many plasma environments, such as Earth's magnetosphere and magnetotail, the wavelength of the waves is too large compared with the probe separations to measure a time delay. This is particularly a problem for axial probes, which have significantly shorter separations than spin-plane probes. The fact that the axial probes are closer to the spacecraft means that they can be strongly influenced by the spacecraft. Overall, this makes estimating time delays from the axial probes extremely difficult, and results can be quite unreliable. The methods are also restricted by the cadence of the probe measurements (8.192 kHz for MMS in burst mode), typically limiting the frequency of the waves that can be investigated to well below the Nyquist frequency.

Recently, the reliability of these three interferometry methods was investigated by Steinvall et al. (2022), using an analytic model. They showed that method (1) is highly susceptible to spacecraft potential fluctuations and how non-planar the wave is. This is particularly important for electron holes, which are highly localized and often non-planar. The spacecraft potential fluctuation effects were found to be reduced for high-density plasmas. Although it was found that method (2) is generally reliable when wave vector direction is known and closely aligned with one of the probe pairs, method (3) was found to be the preferable method to use to determine the spin-plane component of the phase velocity and wave vector.

**Acknowledgements** We thank Shan Wang for her contributions to the sections on lower hybrid waves. We thank the International Space Science Institute (ISSI) for hosting the Magnetic Reconnection: Explosive Energy Conversion in Space Plasmas team. DBG acknowledges support from the Swedish National Space Agency (SNSA), Grant 128/17. GC acknowledges support from the Academy of Finland Grant n.345701. CN acknowledges support from the Research Council of Norway under Contract No. 300865, and SNSA, Grant 2022-00121. LR acknowledges support from SNSA, Grant 139/18. JFD acknowledges support from NSF, Grant PHY2109083, and NASA, Grant 80NSSC22K0352. The work was supported by the Knut and Alice Wallenberg foundation (Dnr. 2022.0087). Figures produced for this paper were generated using the irfu-matlab software package (<https://github.com/irfu/irfu-matlab>). MMS data are publicly available at <https://lasp.colorado.edu/mms/sdc/public>.

**Funding** Open access funding provided by Uppsala University.

## Declarations

**Competing Interests** The authors declare no competing interests.

**Open Access** This article is licensed under a Creative Commons Attribution 4.0 International License, which permits use, sharing, adaptation, distribution and reproduction in any medium or format, as long as you give appropriate credit to the original author(s) and the source, provide a link to the Creative Commons licence, and indicate if changes were made. The images or other third party material in this article are included in the article's Creative Commons licence, unless indicated otherwise in a credit line to the material. If material is not included in the article's Creative Commons licence and your intended use is not permitted by statutory regulation or exceeds the permitted use, you will need to obtain permission directly from the copyright holder. To view a copy of this licence, visit <http://creativecommons.org/licenses/by/4.0/>.



## References

- Angelopoulos V, Chapman JA, Mozer FS, et al (2002) Plasma sheet electromagnetic power generation and its dissipation along auroral field lines. *J Geophys Res Space Phys* 107(A8):SMP 14–1–SMP 14–20. <https://doi.org/10.1029/2001JA900136>
- Angelopoulos V, McFadden JP, Larson D, et al (2008) Tail reconnection triggering substorm onset. *Science* 321(5891):931–935. <https://doi.org/10.1126/science.1160495>
- Artemyev AV, Neishtadt AI, Angelopoulos V (2022) On the role of whistler-mode waves in electron interaction with dipolarizing flux bundles. *J Geophys Res Space Phys* 127(4):e2022JA030265. <https://doi.org/10.1029/2022JA030265>
- Arzner K, Scholer M (2001) Kinetic structure of the post plasmoid plasma sheet during magnetotail reconnection. *J Geophys Res Space Phys* 106(A3):3827–3844. <https://doi.org/10.1029/2000JA000179>
- Bakrania MR, Rae IJ, Walsh AP, et al (2022) Direct evidence of magnetic reconnection onset via the tearing instability. *Front Astron Space Sci* 9:869491. <https://doi.org/10.3389/fspas.2022.869491>
- Bale SD, Mozer FS, Phan T (2002) Observation of lower hybrid drift instability in the diffusion region at a reconnecting magnetopause. *Geophys Res Lett* 29:2180. <https://doi.org/10.1029/2002GL016113>
- Bale SD, Kasper JC, Howes GG, et al (2009) Magnetic fluctuation power near proton temperature anisotropy instability thresholds in the solar wind. *Phys Rev Lett* 103:211101. <https://doi.org/10.1103/PhysRevLett.103.211101>
- Bessho N, Bhattacharjee A (2014) Instability of the current sheet in the Earth's magnetotail with normal magnetic field. *Phys Plasmas* 102:905. <https://doi.org/10.1063/1.4899043>
- Birn J, Hesse M, Runov A (2022) Electron anisotropies in magnetotail dipolarization events. *Front Astron Space Sci* 9:908730. <https://doi.org/10.3389/fspas.2022.908730>
- Burch JL, Torbert RB, Phan TD, et al (2016) Electron-scale measurements of magnetic reconnection in space. *Science* 352(6290):aaf2939. <https://doi.org/10.1126/science.aaf2939>
- Burch J, Dokgo K, Hwang K, et al (2019) High-frequency wave generation in magnetotail reconnection: linear dispersion analysis. *Geophys Res Lett* 46(8):4089–4097. <https://doi.org/10.1029/2019GL082471>
- Burkhart GR, Drake JF, Dusenbery PB, et al (1992) Ion tearing in a magnetotail configuration with an embedded thin current sheet. *J Geophys Res Space Phys* 97:16749–16756. <https://doi.org/10.1029/92JA01523>
- Cairns IH, McMillan BF (2005) Electron acceleration by lower hybrid waves in magnetic reconnection regions. *Phys Plasmas* 12:102110. <https://doi.org/10.1063/1.2080567>
- Cairns IH, Lobzin VV, Donea A, et al (2018) Low altitude solar magnetic reconnection, type III solar radio bursts, and X-ray emissions. *Sci Rep* 8:1676. <https://doi.org/10.1038/s41598-018-19195-3>
- Cao JB, Wei XH, Duan AY, et al (2013) Slow magnetosonic waves detected in reconnection diffusion region in the Earth's magnetotail. *J Geophys Res Space Phys* 118(4):1659–1666. <https://doi.org/10.1002/jgra.50246>
- Cao D, Fu HS, Cao JB, et al (2017) MMS observations of whistler waves in electron diffusion region. *Geophys Res Lett* 44(9):3954–3962. <https://doi.org/10.1002/2017GL072703>
- Capon J (1969) High-resolution frequency-wavenumber spectrum analysis. *Proc IEEE* 57(8):1408–1418. <https://doi.org/10.1109/PROC.1969.7278>
- Carter TA, Ji H, Trintchouk F, et al (2001) Measurement of lower-hybrid drift turbulence in a reconnecting current sheet. *Phys Rev Lett* 88:015001. <https://doi.org/10.1103/PhysRevLett.88.015001>
- Cattell CA, Mozer FS (1986) Experimental determination of the dominant wave mode in the active near-Earth magnetotail. *Geophys Res Lett* 13(3):221–224. <https://doi.org/10.1029/GL013i003p00221>
- Chaston CC, Phan TD, Bonnell JW, et al (2005) Drift-kinetic Alfvén waves observed near a reconnection X line in the Earth's magnetopause. *Phys Rev Lett* 95:065002. <https://doi.org/10.1103/PhysRevLett.95.065002>
- Chaston CC, Johnson JR, Wilber M, et al (2009) Kinetic Alfvén wave turbulence and transport through a reconnection diffusion region. *Phys Rev Lett* 102:015001. <https://doi.org/10.1103/PhysRevLett.102.015001>
- Chaston CC, Bonnell JW, Clausen L, et al (2012) Energy transport by kinetic-scale electromagnetic waves in fast plasma sheet flows. *J Geophys Res Space Phys* 117(A9):A09202. <https://doi.org/10.1029/2012JA017863>
- Che H, Drake JF, Swisdak M, et al (2010) Electron holes and heating in the reconnection dissipation region. *Geophys Res Lett* 37:L11105. <https://doi.org/10.1029/2010GL043608>
- Che H, Drake JF, Swisdak M (2011) A current filamentation mechanism for breaking magnetic field lines during reconnection. *Nature* 474:184–187. <https://doi.org/10.1038/nature10091>
- Chen LJ, Hesse M, et al (2016) Electron energization and mixing observed by MMS in the vicinity of an electron diffusion region during magnetopause reconnection. *Geophys Res Lett* 43:6036–6043. <https://doi.org/10.1002/2016GL069215>

- Chen LJ, Hesse M, Wang S, et al (2017) Electron diffusion region during magnetopause reconnection with an intermediate guide field: magnetospheric multiscale observations. *J Geophys Res Space Phys* 122:5235–5246. <https://doi.org/10.1002/2017JA024004>
- Chen LJ, Wang S, Le Contel O, et al (2020) Lower-hybrid drift waves driving electron nongyrotropic heating and vortical flows in a magnetic reconnection layer. *Phys Rev Lett* 125:025103. <https://doi.org/10.1103/PhysRevLett.125.025103>
- Chen L, Zonca F, Lin Y (2021) Physics of kinetic Alfvén waves: a gyrokinetic theory approach. *Rev Mod Plasma Phys* 5(1):1
- Cheng L, Lin Y, Perez JD, et al (2020) Kinetic Alfvén waves from magnetotail to the ionosphere in global hybrid simulation associated with fast flows. *J Geophys Res Space Phys* 125(2):e2019JA027062. <https://doi.org/10.1029/2019JA027062>
- Chiou SW, Hau LN (2003) Explosive and oscillatory tearing-mode instability in gyrotronic plasmas. *Phys Plasmas* 10(10):3813–3816. <https://doi.org/10.1063/1.1606682>
- Coppi B, Laval G, Pellat R (1966) Dynamics of the geomagnetic tail. *Phys Rev Lett* 16(26):1207–1210. <https://doi.org/10.1103/PhysRevLett.16.1207>
- Cozzani G, Khotyaintsev YV, Graham DB, et al (2021) Structure of a perturbed magnetic reconnection electron diffusion region in the Earth's magnetotail. *Phys Rev Lett* 127:215101. <https://doi.org/10.1103/PhysRevLett.127.215101>
- Cozzani G, Khotyaintsev YV, Graham DB, et al (2023) Direct observations of electron firehose fluctuations in the magnetic reconnection outflow. *J Geophys Res Space Phys* 128(5):e2022JA031128. <https://doi.org/10.1029/2022JA031128>
- Dai L (2009) Collisionless magnetic reconnection via Alfvén eigenmodes. *Phys Rev Lett* 102:245003. <https://doi.org/10.1103/PhysRevLett.102.245003>
- Dai L, Wygant JR, Cattell C, et al (2011) Cluster observations of surface waves in the ion jets from magnetotail reconnection. *J Geophys Res Space Phys* 116(A12):A12227. <https://doi.org/10.1029/2011JA017004>
- Daughton W (1999) The unstable eigenmodes of a neutral sheet. *Phys Plasmas* 6(4):1329–1343. <https://doi.org/10.1063/1.873374>
- Daughton W (2003) Electromagnetic properties of the lower-hybrid drift instability in a thin current sheet. *Phys Plasmas* 10:3103. <https://doi.org/10.1063/1.1594724>
- Davidson RC, Gladd NT, Wu CS, et al (1977) Effects of finite plasma beta on the lower-hybrid-drift instability. *Phys Fluids* 20:301. <https://doi.org/10.1063/1.861867>
- Divin A, Khotyaintsev YV, Vaivads A, et al (2015a) Evolution of the lower hybrid drift instability at reconnection jet front. *J Geophys Res Space Phys* 120(4):2675–2690. <https://doi.org/10.1002/2014JA020503>
- Divin A, Khotyaintsev YV, Vaivads A, et al (2015b) Lower hybrid drift instability at a dipolarization front. *J Geophys Res Space Phys* 120(2):1124–1132. <https://doi.org/10.1002/2014JA020528>
- Dokgo K, Hwang KJ, Burch JL, et al (2019) High-frequency wave generation in magnetotail reconnection: nonlinear harmonics of upper hybrid waves. *Geophys Res Lett* 46(14):7873–7882. <https://doi.org/10.1029/2019GL083361>
- Dokgo K, Hwang KJ, Burch JL, et al (2020a) The effects of upper-hybrid waves on energy dissipation in the electron diffusion region. *Geophys Res Lett* 47(19):e2020GL089778. <https://doi.org/10.1029/2020GL089778>
- Dokgo K, Hwang KJ, Burch JL, et al (2020b) High-frequency waves driven by agyrotropic electrons near the electron diffusion region. *Geophys Res Lett* 47(5):e2020GL087111. <https://doi.org/10.1029/2020GL087111>
- Drake JF, Lee YC (1977) Kinetic theory of tearing instabilities. *Phys Fluids* 20(8):1341–1353. <https://doi.org/10.1063/1.862017>
- Duan SP, Dai L, Wang C, et al (2016) Evidence of kinetic Alfvén eigenmode in the near-Earth magnetotail during substorm expansion phase. *J Geophys Res Space Phys* 121(5):4316–4330. <https://doi.org/10.1002/2016JA022431>
- Eastwood JP, Goldman MV, Hietala H, et al (2015) Ion reflection and acceleration near magnetotail dipolarization fronts associated with magnetic reconnection. *J Geophys Res Space Phys* 120(1):511–525. <https://doi.org/10.1002/2014JA020516>
- Egedal J, Daughton W, Le A, et al (2015) Double layer electric fields aiding the production of energetic flat-top distributions and superthermal electrons within magnetic reconnection exhausts. *Phys Plasmas* 22:101208. <https://doi.org/10.1063/1.4933055>
- Ergun RE, Andersson L, Tao J, et al (2009) Observations of double layers in Earth's plasma sheet. *Phys Rev Lett* 102:155002. <https://doi.org/10.1103/PhysRevLett.102.155002>
- Ergun RE, Holmes JC, Goodrich KA, et al (2016) Magnetospheric multiscale observations of large-amplitude, parallel, electrostatic waves associated with magnetic reconnection at the magnetopause. *Geophys Res Lett* 43:5626–5634. <https://doi.org/10.1002/2016GL068992>

- Ergun RE, Chen LJ, Wilder FD, et al (2017) Drift waves, intense parallel electric fields, and turbulence associated with asymmetric magnetic reconnection at the magnetopause. *Geophys Res Lett* 44:2978–2986. <https://doi.org/10.1002/2016GL072493>
- Ergun RE, Hoilijoki S, Ahmadi N, et al (2019) Magnetic reconnection in three dimensions: observations of electromagnetic drift waves in the adjacent current sheet. *J Geophys Res Space Phys* 124(12):10104–10118. <https://doi.org/10.1029/2019JA027228>
- Erkaev NV, Semenov VS, Biernat HK (2007) Magnetic double-gradient instability and flapping waves in a current sheet. *Phys Rev Lett* 99(23):235003. <https://doi.org/10.1103/PhysRevLett.99.235003>
- Farrell WM, Desch MD, Kaiser ML, et al (2002) The dominance of electron plasma waves near a reconnection X-line region. *Geophys Res Lett* 29:1902. <https://doi.org/10.1029/2002GL014662>
- Farrell WM, Desch MD, Ogilvie KW, et al (2003) The role of upper hybrid waves in magnetic reconnection. *Geophys Res Lett* 30:2259. <https://doi.org/10.1029/2003GL017549>
- Finelli F, Cerri SS, Califano F, et al (2021) Bridging hybrid- and full-kinetic models with Landau-fluid electrons - I. 2D magnetic reconnection. *Astron Astrophys* 653:A156. <https://doi.org/10.1051/0004-6361/202140279>
- Fu HS, Khotyaintsev YV, Vaivads A, et al (2013) Energetic electron acceleration by unsteady magnetic reconnection. *Nat Phys* 9(7):426–430. <https://doi.org/10.1038/nphys2664>
- Fujimoto K (2014) Wave activities in separatrix regions of magnetic reconnection. *Geophys Res Lett* 41:2721. <https://doi.org/10.1002/2014GL059893>
- Fujimoto K, Sydora RD (2008) Whistler waves associated with magnetic reconnection. *Geophys Res Lett* 35:L19112. <https://doi.org/10.1029/2008GL035201>
- Fujimoto M, Shinohara I, Kojima H (2011) Reconnection and waves: a review with a perspective. *Space Sci Rev* 160:123. <https://doi.org/10.1007/s11214-011-9807-7>
- Furth HP, Killeen J, Rosenbluth MN (1963) Finite-resistivity instabilities of a sheet pinch. *Phys Fluids* 6(4):459–484. <https://doi.org/10.1063/1.1706761>
- Galeev AA, Zelený LM (1976) Tearing instability in plasma configurations. *Sov Phys JETP* 43:1113
- Gao JW, Rong ZJ, Cai YH, et al (2018) The distribution of two flapping types of magnetotail current sheet: implication for the flapping mechanism. *J Geophys Res Space Phys* 123(9):7413–7423. <https://doi.org/10.1029/2018JA025695>
- Gary SP (1993) Theory of space plasma microinstabilities. Cambridge atmospheric and space science series. Cambridge University Press, Cambridge. <https://doi.org/10.1017/CBO9780511551512>
- Gary SP, Nishimura K (2003) Resonant electron firehose instability: particle-in-cell simulations. *Phys Plasmas* 10(9):3571–3576. <https://doi.org/10.1063/1.1590982>
- Gary SP, Montgomery MD, Feldman WC, et al (1976) Proton temperature anisotropy instabilities in the solar wind. *J Geophys Res* 81(7):1241–1246. <https://doi.org/10.1029/JA081i007p01241>
- Gary SP, Li H, O'Rourke S, et al (1998) Proton resonant firehose instability: temperature anisotropy and fluctuating field constraints. *J Geophys Res Space Phys* 103(A7):14567–14574. <https://doi.org/10.1029/98JA01174>
- Gary SP, Lavraud B, Thomsen MF, et al (2005) Electron anisotropy constraint in the magnetosheath: cluster observations. *Geophys Res Lett* 32(13):L13109. <https://doi.org/10.1029/2005GL023234>
- Genestreti KJ, Farrugia CJ, Lu S, et al (2023) Multi-scale observation of magnetotail reconnection onset: 2. Microscopic dynamics. *J Geophys Res Space Phys* 128(11):e2023JA031760. <https://doi.org/10.1029/2023JA031760>
- Gershman DJ, F-Viñas A, Dorelli JC, et al (2017) Wave-particle energy exchange directly observed in a kinetic Alfvén-branch wave. *Nat Commun* 8:14719. <https://doi.org/10.1038/ncomms14719>
- Gershman DJ, F-Viñas A, Dorelli JC, et al (2018) Energy partitioning constraints at kinetic scales in low- $\beta$  turbulence. *Phys Plasmas* 25(2):022303. <https://doi.org/10.1063/1.5009158>
- Goldman MV, Newman DL, Lapenta G, et al (2014) Čerenkov emission of quasiparallel whistlers by fast electron phase-space holes during magnetic reconnection. *Phys Rev Lett* 112:145002. <https://doi.org/10.1103/PhysRevLett.112.145002>
- Götz Paschmann PWD (ed) (1998) Analysis methods for multi-spacecraft data. The International Space Science Institute, Chap. 10
- Graham DB, Khotyaintsev YV, Vaivads A, et al (2014) Electron dynamics in the diffusion region of an asymmetric magnetic reconnection. *Phys Rev Lett* 112:215004. <https://doi.org/10.1103/PhysRevLett.112.215004>
- Graham DB, Khotyaintsev YV, Vaivads A, et al (2015) Electrostatic solitary waves with distinct speeds associated with asymmetric reconnection. *Geophys Res Lett* 42:215. <https://doi.org/10.1002/2014GL062538>
- Graham DB, Khotyaintsev YV, Vaivads A, et al (2016a) Electrostatic solitary waves and electrostatic waves at the magnetopause. *J Geophys Res Space Phys* 121:3069–3092. <https://doi.org/10.1002/2015JA021527>

- Graham DB, Vaivads A, Khotyaintsev YV, et al (2016b) Whistler emission in the separatrix regions of asymmetric reconnection. *J Geophys Res* 121:1934–1954. <https://doi.org/10.1002/2015JA021239>
- Graham DB, Khotyaintsev YV, Norgren C, et al (2017a) Lower hybrid waves in the ion diffusion and magnetospheric inflow regions. *J Geophys Res Space Phys*. <https://doi.org/10.1002/2016JA023572>
- Graham DB, Khotyaintsev YV, Vaivads A, et al (2017b) Instability of agyrotropic electron beams near the electron diffusion region. *Phys Rev Lett* 119:025101. <https://doi.org/10.1103/PhysRevLett.119.025101>
- Graham DB, Khotyaintsev YV, Norgren C, et al (2019) Universality of lower hybrid waves at Earth's magnetopause. *J Geophys Res Space Phys* 124(11):8727–8760. <https://doi.org/10.1029/2019JA027155>
- Graham DB, Khotyaintsev YV, André M, et al (2021) Non-maxwellianity of electron distributions near Earth's magnetopause. *J Geophys Res Space Phys* 126(10):e2021JA029260. <https://doi.org/10.1029/2021JA029260>
- Graham DB, Khotyaintsev YV, André M, et al (2022) Direct observations of anomalous resistivity and diffusion in collisionless plasma. *Nat Commun* 13:2954. <https://doi.org/10.1038/s41467-022-30561-8>
- Graham DB, Khotyaintsev YV, André M (2023) Langmuir and upper hybrid waves in Earth's magnetotail. *J Geophys Res Space Phys* 128(10):e2023JA031900. <https://doi.org/10.1029/2023JA031900>
- Greco A, Artemyev A, Zimbardo G, et al (2017) Role of lower hybrid waves in ion heating at dipolarization fronts. *J Geophys Res Space Phys* 122(5):5092–5104. <https://doi.org/10.1002/2017JA023926>
- Grigorenko EE, Malykhin AY, Kronberg EA, et al (2023) Quasi-parallel whistler waves and their interaction with resonant electrons during high-velocity bulk flows in the Earth's magnetotail. *Astrophys J* 943(2):169. <https://doi.org/10.3847/1538-4357/acaf52>
- Gurram H, Egedal J, Daughton W (2021) Shear Alfvén waves driven by magnetic reconnection as an energy source for the aurora borealis. *Geophys Res Lett* 48(14):e2021GL094201. <https://doi.org/10.1029/2021GL094201>
- Guzdar PN, Hassam AB, Swisdak M, et al (2010) A simple mhd model for the formation of multiple dipolarization fronts. *Geophys Res Lett* 37(20):L20102. <https://doi.org/10.1029/2010GL045017>
- Hasegawa A, Chen L (1976) Kinetic processes in plasma heating by resonant mode conversion of Alfvén wave. *Phys Fluids* 19(12):1924–1934. <https://doi.org/10.1063/1.861427>
- Hau LN, Chen GW, Chang CK (2020) Mirror mode waves immersed in magnetic reconnection. *Astrophys J Lett* 903(1):L12. <https://doi.org/10.3847/2041-8213/abbf4a>
- Hellinger P, Matsumoto H (2000) New kinetic instability: oblique Alfvén fire hose. *J Geophys Res Space Phys* 105(A5):10519–10526. <https://doi.org/10.1029/1999JA000297>
- Hellinger P, Trávníček P, Kasper JC, et al (2006) Solar wind proton temperature anisotropy: linear theory and wind/swe observations. *Geophys Res Lett* 33(9):L09101. <https://doi.org/10.1029/2006GL025925>
- Hesse M, Schindler K (2001) The onset of magnetic reconnection in the magnetotail. *Earth Planets Space* 53:645–653
- Hesse M, Norgren C, Tenfjord P, et al (2018) On the role of separatrix instabilities in heating the reconnection outflow region. *Phys Plasmas* 25(12):122902. <https://doi.org/10.1063/1.5054100>
- Hietala H, Drake JF, Phan TD, et al (2015) Ion temperature anisotropy across a magnetotail reconnection jet. *Geophys Res Lett* 42(18):7239–7247. <https://doi.org/10.1002/2015GL065168>
- Higashimori K, Hoshino M (2015) Ion beta dependence on the development of Alfvénic fluctuations in reconnection jets. *J Geophys Res Space Phys* 120(3):1803–1813. <https://doi.org/10.1002/2014JA020544>
- Hoilijoki S, Ganse U, Pfau-Kempf Y, et al (2017) Reconnection rates and X line motion at the magnetopause: global 2D-3V hybrid-Vlasov simulation results. *J Geophys Res Space Phys* 122(3):2877–2888. <https://doi.org/10.1002/2016JA023709>
- Hollweg JV, Völk HJ (1970) New plasma instabilities in the solar wind. *J Geophys Res* 75(28):5297–5309. <https://doi.org/10.1029/JA075i028p05297>
- Holmes JC, Ergun RE, Newman DL, et al (2018a) Electron phase-space holes in three dimensions: multi-spacecraft observations by magnetospheric multiscale. *J Geophys Res Space Phys* 123(12):9963–9978. <https://doi.org/10.1029/2018JA025750>
- Holmes JC, Ergun RE, Newman DL, et al (2018b) Negative potential solitary structures in the magnetosheath with large parallel width. *J Geophys Res Space Phys* 123(1):132–145. <https://doi.org/10.1002/2017JA024890>
- Holmes JC, Ergun RE, Nakamura R, et al (2019) Structure of electron-scale plasma mixing along the day-side reconnection separatrix. *J Geophys Res Space Phys* 124(11):8788–8803. <https://doi.org/10.1029/2019JA026974>
- Holmes JC, Nakamura R, Schmid D, et al (2021) Wave activity in a dynamically evolving reconnection separatrix. *J Geophys Res Space Phys* 126(7):e2020JA028520. <https://doi.org/10.1029/2020JA028520>
- Hosner M, Nakamura R, Nakamura TKM, et al (2022) Statistical investigation of electric field fluctuations around the lower-hybrid frequency range at dipolarization fronts in the near-Earth magnetotail. *Phys Plasmas* 29(1):012111. <https://doi.org/10.1063/5.0067382>

- Huang SY, Zhou M, Sahraoui F, et al (2012) Observations of turbulence within reconnection jet in the presence of guide field. *Geophys Res Lett* 39(11):L11104. <https://doi.org/10.1029/2012GL052210>
- Huang SY, Fu HS, Yuan ZG, et al (2016) Two types of whistler waves in the Hall reconnection region. *J Geophys Res Space Phys* 121(7):6639–6646. <https://doi.org/10.1002/2016JA022650>
- Huang H, Yu Y, Dai L, et al (2018) Kinetic Alfvén waves excited in two-dimensional magnetic reconnection. *J Geophys Res Space Phys* 123(8):6655–6669. <https://doi.org/10.1029/2017JA025071>
- Hull AJ, Muschietti L, Le Contel O, et al (2020) Mms observations of intense whistler waves within Earth's supercritical bow shock: source mechanism and impact on shock structure and plasma transport. *J Geophys Res Space Phys* 125(7):e2019JA027290. <https://doi.org/10.1029/2019JA027290>
- Hwang KJ, Goldstein ML, Lee E, et al (2011) Cluster observations of multiple dipolarization fronts. *J Geophys Res Space Phys* 116:A00132. <https://doi.org/10.1029/2010JA015742>
- Hwang KJ, Goldstein ML, F-Viñas A, et al (2014) Wave-particle interactions during a dipolarization front event. *J Geophys Res Space Phys* 119(4):2484–2493. <https://doi.org/10.1002/2013JA019259>
- Ibscher D, Lazar M, Schlickeiser R (2012) On the existence of weibel instability in a magnetized plasma. II. Perpendicular wave propagation: the ordinary mode. *Phys Plasmas* 19(7):072116. <https://doi.org/10.1063/1.4736992>
- Jara-Almonte J, Daughton W, Ji H (2014) Debye scale turbulence within the electron diffusion layer during magnetic reconnection. *Phys Plasmas* 21:032114. <https://doi.org/10.1063/1.4867868>
- Ji H, Terry S, Yamada M, et al (2004) Electromagnetic fluctuations during fast reconnection in a laboratory plasma. *Phys Rev Lett* 92:115001. <https://doi.org/10.1103/PhysRevLett.92.115001>
- Ji H, Kulsrud R, Fox W, et al (2005) An obliquely propagating electromagnetic drift instability in the lower hybrid frequency range. *J Geophys Res Space Phys* 110(A8):A08212. <https://doi.org/10.1029/2005JA011188>
- Ji H, Yoo J, Fox W, et al (2023) Laboratory study of collisionless magnetic reconnection. *Space Sci Rev* 219(8):76. <https://doi.org/10.1007/s11214-023-01024-3>
- Kamaletdinov SR, Hutchinson IH, Vasko IY, et al (2021) Spacecraft observations and theoretical understanding of slow electron holes. *Phys Rev Lett* 127:165101. <https://doi.org/10.1103/PhysRevLett.127.165101>
- Karimabadi H, Krauss-Varban D, Omid N, et al (1999) Magnetic structure of the reconnection layer and core field generation in plasmoids. *J Geophys Res Space Phys* 104(A6):12313–12326. <https://doi.org/10.1029/1999JA900089>
- Karimabadi H, Pritchett PL, Daughton W, et al (2003) Ion-ion kink instability in the magnetotail: 2. Three-dimensional full particle and hybrid simulations and comparison with observations. *J Geophys Res Space Phys* 108(A11):1401. <https://doi.org/10.1029/2003JA010109>
- Kennel CF, Petschek HE (1966) Limit on stably trapped particle fluxes. *J Geophys Res* 71:1–28. <https://doi.org/10.1029/JZ071i001p00001>
- Khotyaintsev Y, Vaivads A, Ogawa Y, et al (2004) Cluster observations of high-frequency waves in the exterior cusp. *Ann Geophys* 22:2403–2411. <https://doi.org/10.5194/angeo-22-2403-2004>
- Khotyaintsev YV, Cully CM, Vaivads A, et al (2011) Plasma jet braking: energy dissipation and nonadiabatic electrons. *Phys Rev Lett* 106:165001. <https://doi.org/10.1103/PhysRevLett.106.165001>
- Khotyaintsev YV, Graham DB, Norgren C, et al (2016) Electron jet of asymmetric reconnection. *Geophys Res Lett* 43:5571–5580. <https://doi.org/10.1002/2016GL069064>
- Khotyaintsev YV, Graham DB, Norgren C, et al (2019) Collisionless magnetic reconnection and waves: progress review. *Front Astron Space Sci* 6:70. <https://doi.org/10.3389/fspas.2019.00070>
- Khotyaintsev YV, Graham DB, Steinvaill K, et al (2020) Electron heating by debye-scale turbulence in guide-field reconnection. *Phys Rev Lett* 124:045101. <https://doi.org/10.1103/PhysRevLett.124.045101>
- Kitamura N, Amano T, Omura Y, et al (2022) Direct observations of energy transfer from resonant electrons to whistler-mode waves in magnetosheath of Earth. *Nat Commun* 13:6259. <https://doi.org/10.1038/s41467-022-33604-2>
- Kleva RG, Drake JF (1984) Stochastic  $E \times B$  particle transport. *Phys Fluids* 27(7):1686–1698. <https://doi.org/10.1063/1.864823>
- Laitinen TV, Khotyaintsev YV, André M, et al (2010) Local influence of the magnetosheath plasma beta fluctuations on magnetopause reconnection. *Ann Geophys* 28:1053
- Lakhina GS, Singh SV, Rubia R (2021) A mechanism for electrostatic solitary waves observed in the reconnection jet region of the Earth's magnetotail. *Adv Space Res* 68(4):1864–1875. <https://doi.org/10.1016/j.asr.2021.04.026>
- Lapenta G, Bettarini L (2011) Self-consistent seeding of the interchange instability in dipolarization fronts. *Geophys Res Lett* 38(11):L11102. <https://doi.org/10.1029/2011GL047742>
- Lapenta G, Goldman M, Newman D, et al (2014) Electromagnetic energy conversion in downstream fronts from three dimensional kinetic reconnection. *Phys Plasmas* 21(5):055702. <https://doi.org/10.1063/1.4872028>



- Lapenta G, Pucci F, Olshevsky V, et al (2018) Nonlinear waves and instabilities leading to secondary reconnection in reconnection outflows. *J Plasma Phys* 84(1):715840103. <https://doi.org/10.1017/S002237781800003X>
- Le Contel O, Roux A, Jacquey C, et al (2009) Quasi-parallel whistler mode waves observed by themis during near-Earth dipolarizations. *Ann Geophys* 27(6):2259–2275. <https://doi.org/10.5194/angeo-27-2259-2009>
- Le Contel O, Retinò A, Breuillard H, et al (2016) Whistler mode waves and Hall fields detected by mms during a dayside magnetopause crossing. *Geophys Res Lett* 43(12):5943–5952. <https://doi.org/10.1002/2016GL068968>
- Le Contel O, Nakamura R, Breuillard H, et al (2017) Lower hybrid drift waves and electromagnetic electron space-phase holes associated with dipolarization fronts and field-aligned currents observed by the magnetospheric multiscale mission during a substorm. *J Geophys Res Space Phys* 122(12):12236–12257. <https://doi.org/10.1002/2017JA024550>
- Le A, Daughton W, Chen LJ, et al (2017) Enhanced electron mixing and heating in 3-D asymmetric reconnection at the Earth's magnetopause. *Geophys Res Lett* 44:2096–2104. <https://doi.org/10.1002/2017GL072522>
- Le A, Daughton W, Ohia O, et al (2018) Drift turbulence, particle transport, and anomalous dissipation at the reconnecting magnetopause. *Phys Plasmas* 25:062103. <https://doi.org/10.1063/1.5027086>
- Le A, Stanier A, Daughton W, et al (2019) Three-dimensional stability of current sheets supported by electron pressure anisotropy. *Phys Plasmas* 26(10):102114. <https://doi.org/10.1063/1.5125014>
- Lembege B, Pellat R (1982) Stability of a thick two-dimensional quasineutral sheet. *Phys Fluids* 25(11):1995–2004. <https://doi.org/10.1063/1.863677>
- Li H, Zhou M, Deng X, et al (2015) A statistical study on the whistler waves behind dipolarization fronts. *J Geophys Res Space Phys* 120(2):1086–1095. <https://doi.org/10.1002/2014JA020474>
- Li WY, Graham DB, Khotyaintsev YV, et al (2020) Electron Bernstein waves driven by electron crescents near the electron diffusion region. *Nat Commun* 11:141. <https://doi.org/10.1038/s41467-019-13920-w>
- Li WY, Khotyaintsev YV, Tang BB, et al (2021) Upper-hybrid waves driven by meandering electrons around magnetic reconnection x line. *Geophys Res Lett* 48(16):e2021GL093164. <https://doi.org/10.1029/2021GL093164>
- Liang J, Lin Y, Johnson JR, et al (2016) Kinetic Alfvén waves in three-dimensional magnetic reconnection. *J Geophys Res Space Phys* 121(7):6526–6548. <https://doi.org/10.1002/2016JA022505>
- Liang J, Lin Y, Johnson JR, et al (2017) Ion acceleration and heating by kinetic Alfvén waves associated with magnetic reconnection. *Phys Plasmas* 24(10):102110. <https://doi.org/10.1063/1.4991978>
- Lin D, Scales WA, Ganguli G, et al (2019) A new perspective for dipolarization front dynamics: electromagnetic effects of velocity inhomogeneity. *J Geophys Res Space Phys* 124(9):7533–7542. <https://doi.org/10.1029/2019JA026815>
- Liu YH, Drake JF, Swisdak M (2012) The structure of the magnetic reconnection exhaust boundary. *Phys Plasmas* 19(2):022110. <https://doi.org/10.1063/1.3685755>
- Liu YH, Birn J, Daughton W, et al (2014) Onset of reconnection in the near magnetotail: pic simulations. *J Geophys Res Space Phys* 119(12):9773–9789. <https://doi.org/10.1002/2014JA020492>
- Liu CM, Vaivads A, Graham DB, et al (2019) Ion-beam-driven intense electrostatic solitary waves in reconnection jet. *Geophys Res Lett* 46(22):12702–12710. <https://doi.org/10.1029/2019GL085419>
- Liu ZY, Zong QG, Rankin R, et al (2023) Particle-sounding of the spatial structure of kinetic Alfvén waves. *Nat Commun* 14(1):2088. <https://doi.org/10.1038/s41467-023-37881-3>
- Lotekar A, Vasko IY, Mozer FS, et al (2020) Multisatellite mms analysis of electron holes in the Earth's magnetotail: origin, properties, velocity gap, and transverse instability. *J Geophys Res Space Phys* 125(9):e2020JA028066. <https://doi.org/10.1029/2020JA028066>
- Lottermoser RF, Scholer M, Matthews AP (1998) Ion kinetic effects in magnetic reconnection: hybrid simulations. *J Geophys Res Space Phys* 103(A3):4547–4559. <https://doi.org/10.1029/97JA01872>
- Lu S, Wang R, Lu Q, et al (2020) Magnetotail reconnection onset caused by electron kinetics with a strong external driver. *Nat Commun* 11:5049. <https://doi.org/10.1038/s41467-020-18787-w>
- Lui ATY, Meng CI, Akasofu SI (1978) Wavy nature of the magnetotail neutral sheet. *Geophys Res Lett* 5(4):279–282. <https://doi.org/10.1029/GL005i004p00279>
- Maruca BA, Chasapis A, Gary SP, et al (2018) Mms observations of beta-dependent constraints on ion temperature anisotropy in Earth's magnetosheath. *Astrophys J* 866(1):25. <https://doi.org/10.3847/1538-4357/aaaddfb>
- Matteini L, Hellinger P, Goldstein BE, et al (2013a) Signatures of kinetic instabilities in the solar wind. *J Geophys Res Space Phys* 118(6):2771–2782. <https://doi.org/10.1002/jgra.50320>
- Matteini L, Landi S, Velli M, et al (2013b) Proton temperature anisotropy and magnetic reconnection in the solar wind: effects of kinetic instabilities on current sheet stability. *Astrophys J* 763(2):142. <https://doi.org/10.1088/0004-637x/763/2/142>



- Motschmann U, Woodward TI, Glassmeier KH, et al (1996) Wavelength and direction filtering by magnetic measurements at satellite arrays: generalized minimum variance analysis. *J Geophys Res Space Phys* 101(A3):4961–4965. <https://doi.org/10.1029/95JA03471>
- Mozer FS, Bale SD, Phan TD (2002) Evidence of diffusion regions at a subsolar magnetopause crossing. *Phys Rev Lett* 89:015002
- Mozer FS, Wilber M, Drake JF (2011) Wave associated anomalous drag during magnetic field reconnection. *Phys Plasmas* 18:102902. <https://doi.org/10.1063/1.3647508>
- Mozer FS, Agapitov OV, Giles B, et al (2018) Direct observation of electron distributions inside millisecond duration electron holes. *Phys Rev Lett* 121:135102. <https://doi.org/10.1103/PhysRevLett.121.135102>
- Muñoz PA, Büchner J (2018) Kinetic turbulence in fast three-dimensional collisionless guide-field magnetic reconnection. *Phys Rev E* 98:043205. <https://doi.org/10.1103/PhysRevE.98.043205>
- Nakamura MS, Matsumoto H, Fujimoto M (2002) Interchange instability at the leading part of reconnection jets. *Geophys Res Lett* 29(8):88–1–88–4. <https://doi.org/10.1029/2001GL013780>
- Nakamura TKM, Nakamura R, Baumjohann W, et al (2016) Three-dimensional development of front region of plasma jets generated by magnetic reconnection. *Geophys Res Lett* 43(16):8356–8364. <https://doi.org/10.1002/2016GL070215>
- Nakamura TKM, Umeda T, Nakamura R, et al (2019) Disturbance of the front region of magnetic reconnection outflow jets due to the lower-hybrid drift instability. *Phys Rev Lett* 123:235101. <https://doi.org/10.1103/PhysRevLett.123.235101>
- Narita Y, Plaschke F, Nakamura R, et al (2016) Wave telescope technique for mms magnetometer. *Geophys Res Lett* 43(10):4774–4780. <https://doi.org/10.1002/2016GL069035>
- Narita Y, Glassmeier KH, Motschmann U (2022) The wave telescope technique. *J Geophys Res Space Phys* 127(2):e2021JA030165. <https://doi.org/10.1029/2021JA030165>
- Ng J, Chen LJ, Le A, et al (2020) Lower-hybrid-drift vortices in the electron-scale magnetic reconnection layer. *Geophys Res Lett* 47(22):e2020GL090726. <https://doi.org/10.1029/2020GL090726>
- Ng J, Yoo J, Chen LJ, et al (2023) 3D simulation of lower-hybrid drift waves in strong guide field asymmetric reconnection in laboratory experiments. *Phys Plasmas* 30(4):042101. <https://doi.org/10.1063/5.0138278>
- Norgren C, Vaivads A, Khotyaintsev YV, et al (2012) Lower hybrid drift waves: space observations. *Phys Rev Lett* 109:055001. <https://doi.org/10.1103/PhysRevLett.109.055001>
- Norgren C, André M, Graham DB, et al (2015) Slow electron holes in multicomponent plasmas. *Geophys Res Lett* 42:7264. <https://doi.org/10.1002/2015GL065390>
- Norgren C, Graham DB, Khotyaintsev YV, et al (2016) Finite gyroradius effects in the electron outflow of asymmetric magnetic reconnection. *Geophys Res Lett* 43:6724–6733. <https://doi.org/10.1002/2016GL069205>
- Norgren C, Hesse M, Graham DB, et al (2020) Electron acceleration and thermalization at magnetotail separatrix. *J Geophys Res Space Phys* 125(4):e2019JA027440. <https://doi.org/10.1029/2019JA027440>
- Norgren C, Graham DB, Argall MR, et al (2022) Millisecond observations of nonlinear wave–electron interaction in electron phase space holes. *Phys Plasmas* 29(1):012309. <https://doi.org/10.1063/5.0073097>
- Norgren C, Chen LJ, Graham DB, et al (2025) Electron and ion dynamics in reconnection diffusion regions. *Space Sci Rev* 221
- Nykyri K, Ma X, Johnson J (2021) Cross-scale energy transport in space plasmas. In: Maggiolo R et al (eds) *Magnetospheres in the Solar System*. Wiley, American Geophysical Union, Chap. 7, pp 109–121. <https://doi.org/10.1002/9781119815624.ch7>
- Øieroset M, Phan TD, Haggerty C, et al (2016) MMS observations of large guide field symmetric reconnection between colliding reconnection jets at the center of a magnetic flux rope at the magnetopause. *Geophys Res Lett* 43:5536–5544. <https://doi.org/10.1002/2016GL069166>
- Pan DX, Khotyaintsev YV, Graham DB, et al (2018) Rippled electron-scale structure of a dipolarization front. *Geophys Res Lett* 45(22):12116–12124. <https://doi.org/10.1029/2018GL080826>
- Pedersen A, Lybekk B, André M, et al (2008) Electron density estimates derived from spacecraft potential measurements on cluster in tenuous plasma regions. *J Geophys Res* 113:A07S33
- Pincon JL, Lefeuvre F (1991) Local characterization of homogeneous turbulence in a space plasma from simultaneous measurements of field components at several points in space. *J Geophys Res Space Phys* 96(A2):1789–1802. <https://doi.org/10.1029/90JA02183>
- Price L, Swisdak M, Drake JF, et al (2016) The effects of turbulence on three-dimensional magnetic reconnection at the magnetopause. *Geophys Res Lett* 43:6020–6027. <https://doi.org/10.1002/2016GL069578>
- Price L, Swisdak M, Drake JF, et al (2017) Turbulence in three-dimensional simulations of magnetopause reconnection. *J Geophys Res Space Phys* 122:11086–11099. <https://doi.org/10.1002/2017JA024227>
- Price L, Swisdak M, Drake JF, et al (2020) Turbulence and transport during guide field reconnection at the magnetopause. *J Geophys Res Space Phys* 125(4):e2019JA027498. <https://doi.org/10.1029/2019JA027498>

- Pritchett PL (2005) Externally driven magnetic reconnection in the presence of a normal magnetic field. *J Geophys Res Space Phys* 110(A5):A05209. <https://doi.org/10.1029/2004JA010948>
- Pritchett PL (2013) The influence of intense electric fields on three-dimensional asymmetric magnetic reconnection. *Phys Plasmas* 20:061204. <https://doi.org/10.1063/1.4811123>
- Pritchett PL (2015a) Instability of current sheets with a localized accumulation of magnetic flux. *Phys Plasmas* 22(6):062102. <https://doi.org/10.1063/1.4921666>
- Pritchett PL (2015b) Structure of exhaust jets produced by magnetic reconnection localized in the out-of-plane direction. *J Geophys Res Space Phys* 120(1):592–608. <https://doi.org/10.1002/2014JA020795>
- Rager AC, Dorelli JC, Gershman DJ, et al (2018) Electron crescent distributions as a manifestation of diamagnetic drift in an electron-scale current sheet: magnetospheric multiscale observations using new 7.5 ms fast plasma investigation moments. *Geophys Res Lett* 45(2):578–584. <https://doi.org/10.1002/2017GL076260>
- Ren Y, Dai L, Li W, et al (2019) Whistler waves driven by field-aligned streaming electrons in the near-Earth magnetotail reconnection. *Geophys Res Lett* 46(10):5045–5054. <https://doi.org/10.1029/2019GL083283>
- Ren Y, Dai L, Wang C, et al (2022) Parallel electron heating through Landau resonance with lower hybrid waves at the edge of reconnection ion jets. *Astrophys J* 928(1):5. <https://doi.org/10.3847/1538-4357/ac53fb>
- Retinò A, Vaivads A, André M, et al (2006) Structure of the separatrix region close to a magnetic reconnection X-line: cluster observations. *Geophys Res Lett* 33:L06101. <https://doi.org/10.1029/2005GL024650>
- Révillé V, Velli M, Rouillard AP, et al (2020) Tearing instability and periodic density perturbations in the slow solar wind. *Astrophys J Lett* 895(1):L20. <https://doi.org/10.3847/2041-8213/ab911d>
- Richard L, Khotyaintsev YV, Graham DB, et al (2021) Observations of short-period ion-scale current sheet flapping. *J Geophys Res Space Phys* 126(8):e29152. <https://doi.org/10.1029/2021JA029152>
- Richard L, Khotyaintsev YV, Graham DB, et al (2023) Fast ion isotropization by current sheet scattering in magnetic reconnection jets. *Phys Rev Lett* 131:115201. <https://doi.org/10.1103/PhysRevLett.131.115201>
- Roberts OW, Narita Y, Li X, et al (2017) Multipoint analysis of compressive fluctuations in the fast and slow solar wind. *J Geophys Res Space Phys* 122(7):6940–6963. <https://doi.org/10.1002/2016JA023552>
- Rogers BN, Denton RE, Drake JF, et al (2001) Role of dispersive waves in collisionless magnetic reconnection. *Phys Rev Lett* 87:195004. <https://doi.org/10.1103/PhysRevLett.87.195004>
- Roytershteyn V, Daughton W, Karimabadi H, et al (2012) Influence of the lower-hybrid drift instability on magnetic reconnection in asymmetric configurations. *Phys Rev Lett* 108:185001. <https://doi.org/10.1103/PhysRevLett.108.185001>
- Runov A, Nakamura R, Baumjohann W, et al (2003) Cluster observation of a bifurcated current sheet. *Geophys Res Lett* 30(2):1036. <https://doi.org/10.1029/2002GL016136>
- Runov A, Sergeev VA, Baumjohann W, et al (2005) Electric current and magnetic field geometry in flapping magnetotail current sheets. *Ann Geophys* 23(4):1391–1403. <https://doi.org/10.5194/angeo-23-1391-2005>
- Schindler K (1972) A self-consistent theory of the tail of the magnetosphere. In: McCormac BM (ed) *Earth's magnetospheric processes*, p 200. [https://doi.org/10.1007/978-94-010-2896-7\\_19](https://doi.org/10.1007/978-94-010-2896-7_19)
- Schindler K (1974) A theory of the substorm mechanism. *J Geophys Res* 79(19):2803–2810. <https://doi.org/10.1029/JA079i019p02803>
- Sergeev V, Runov A, Baumjohann W, et al (2004) Orientation and propagation of current sheet oscillations. *Geophys Res Lett* 31(5):L05807. <https://doi.org/10.1029/2003GL019346>
- Sharma Pyakurel P, Shay MA, Haggerty CC, et al (2018) Super-Alfvénic propagation and damping of reconnection onset signatures. *J Geophys Res Space Phys* 123(1):341–349. <https://doi.org/10.1002/2017JA024606>
- Shay MA, Drake JF, Eastwood JP, et al (2011) Super-Alfvénic propagation of substorm reconnection signatures and Poynting flux. *Phys Rev Lett* 107:065001. <https://doi.org/10.1103/PhysRevLett.107.065001>
- Shi F, Lin Y, Wang X (2013) Global hybrid simulation of mode conversion at the dayside magnetopause. *J Geophys Res Space Phys* 118(10):6176–6187. <https://doi.org/10.1002/jgra.50587>
- Shi P, Huang K, Lu Q, et al (2019) Experimental observation of kinetic Alfvén wave generated by magnetic reconnection. *Plasma Phys Control Fusion* 61(12):125010. <https://doi.org/10.1088/1361-6587/ab4f9c>
- Sitnov MI, Schindler K (2010) Tearing stability of a multiscale magnetotail current sheet. *Geophys Res Lett* 37(8):L08102. <https://doi.org/10.1029/2010GL042961>
- Sitnov MI, Swisdak M, Drake JF, et al (2004) A model of the bifurcated current sheet: 2. Flapping motions. *Geophys Res Lett* 31(9):L09805. <https://doi.org/10.1029/2004GL019473>
- Sitnov MI, Buzulukova N, Swisdak M, et al (2013) Spontaneous formation of dipolarization fronts and reconnection onset in the magnetotail. *Geophys Res Lett* 40(1):22–27. <https://doi.org/10.1029/2012GL054701>






- Sitnov MI, Merkin VG, Swisdak M, et al (2014) Magnetic reconnection, buoyancy, and flapping motions in magnetotail explosions. *J Geophys Res Space Phys* 119(9):7151–7168. <https://doi.org/10.1002/2014JA020205>
- Sitnov M, Birn J, Ferdousi B, et al (2019) Explosive magnetotail activity. *Space Sci Rev* 215(4):31. <https://doi.org/10.1007/s11214-019-0599-5>
- Speiser TW (1973) Magnetospheric current sheets. *Radio Sci* 8(11):973–977. <https://doi.org/10.1029/RS008i011p00973>
- Speiser TW, Ness NF (1967) The neutral sheet in the geomagnetic tail: its motion, equivalent currents, and field line connection through it. *J Geophys Res* 72(1):131–141. <https://doi.org/10.1029/JZ072i001p00131>
- Stasiewicz K, Bellan P, Chaston C, et al (2000) Small scale Alfvénic structure in the aurora. *Space Sci Rev* 92(3):423–533. <https://doi.org/10.1023/A:1005207202143>
- Stawarz JE, Eastwood JP, Varsani A, et al (2017) Magnetospheric multiscale analysis of intense field-aligned Poynting flux near the Earth's plasma sheet boundary. *Geophys Res Lett* 44(14):7106–7113. <https://doi.org/10.1002/2017GL073685>
- Stawarz JE, Muñoz PA, Bessho N, et al (2024) The interplay between collisionless magnetic reconnection and turbulence. *Space Sci Rev* 220:90. <https://doi.org/10.1007/s11214-024-01124-8>
- Steinvall K, Khotyaintsev YV, Graham DB, et al (2019a) Observations of electromagnetic electron holes and evidence of Cherenkov whistler emission. *Phys Rev Lett* 123:255101. <https://doi.org/10.1103/PhysRevLett.123.255101>
- Steinvall K, Khotyaintsev YV, Graham DB, et al (2019b) Multispacecraft analysis of electron holes. *Geophys Res Lett* 46(1):55–63. <https://doi.org/10.1029/2018GL080757>
- Steinvall K, Khotyaintsev YV, Graham DB, et al (2021) Large amplitude electrostatic proton plasma frequency waves in the magnetospheric separatrix and outflow regions during magnetic reconnection. *Geophys Res Lett* 48(5):e2020GL090286. <https://doi.org/10.1029/2020GL090286>
- Steinvall K, Khotyaintsev YV, Graham DB (2022) On the applicability of single-spacecraft interferometry methods using electric field probes. *J Geophys Res Space Phys* 127(3):e2021JA030143. <https://doi.org/10.1029/2021JA030143>
- Stix TH (1992) The theory of plasma waves. American Institute of Physics, Melville
- Stringer TE (1964) Electrostatic instabilities in current-carrying and counterstreaming plasmas. *J Nucl Energy, Part C Plasma Phys Accel Thermonucl Res* 6(3):267–279. <https://doi.org/10.1088/0368-3281/6/3/305>
- Swanson DG (1989) Plasma waves. Academic Press, Boston
- TanDokoro R, Fujimoto M (2005) Three-dimensional mhd simulation study of the structure at the leading part of a reconnection jet. *Geophys Res Lett* 32(23):L23102. <https://doi.org/10.1029/2005GL024467>
- Tang BB, Li WY, Graham DB, et al (2020a) Lower hybrid waves at the magnetosheath separatrix region. *Geophys Res Lett* 47(20):e2020GL089880. <https://doi.org/10.1029/2020GL089880>
- Tang BB, Li WY, Le A, et al (2020b) Electron mixing and isotropization in the exhaust of asymmetric magnetic reconnection with a guide field. *Geophys Res Lett* 47(14):e2020GL087159. <https://doi.org/10.1029/2020GL087159>
- Taroyan Y, Erdélyi R (2002) Resonant and Kelvin–Helmholtz instabilities on the magnetopause. *Phys Plasmas* 9(7):3121–3129. <https://doi.org/10.1063/1.1481746>
- Tjulin A, Pincon JL, Sahraoui F, et al (2005) The k-filtering technique applied to wave electric and magnetic field measurements from the cluster satellites. *J Geophys Res Space Phys* 110(A11):A11224. <https://doi.org/10.1029/2005JA011125>
- Tong Y, Vasko I, Mozer FS, et al (2018) Simultaneous multispacecraft probing of electron phase space holes. *Geophys Res Lett* 45(21):11513–11519. <https://doi.org/10.1029/2018GL079044>
- Torbert RB, Burch JL, Phan TD, et al (2018) Electron-scale dynamics of the diffusion region during symmetric magnetic reconnection in space. *Science* 362(6421):1391–1395. <https://doi.org/10.1126/science.aat2998>
- Treumann RA, Baumjohann W (1997) Advanced space plasma physics. Imperial College Press, London
- Tsai E, Artemyev A, Zhang XJ, et al (2022) Relativistic electron precipitation driven by nonlinear resonance with whistler-mode waves. *J Geophys Res Space Phys* 127(5):e30338. <https://doi.org/10.1029/2022JA030338>
- Uchino H, Kurita S, Harada Y, et al (2017) Waves in the innermost open boundary layer formed by dayside magnetopause reconnection. *J Geophys Res Space Phys* 122(3):3291–3307. <https://doi.org/10.1002/2016JA023300>
- Vaivads A, André M, Buchert SC, et al (2004) Cluster observations of lower hybrid turbulence within thin layers at the magnetopause. *Geophys Res Lett* 31:L03804. <https://doi.org/10.1029/2003GL018142>
- Vaivads A, Khotyaintsev Y, André M, et al (2006) Plasma waves near reconnection sites. In: LaBelle JW, Treumann RA (eds) Geospace electromagnetic waves and radiation. Lecture Notes in Physics, vol 687. Springer, Berlin, Heidelberg, pp 251–269. [https://doi.org/10.1007/3-540-33203-0\\_10](https://doi.org/10.1007/3-540-33203-0_10)





- Vapirev A, Lapenta G, Divin A, et al (2013) Formation of a transient front structure near reconnection point in 3-d pic simulations. *J Geophys Res Space Phys* 118(4):1435–1449. <https://doi.org/10.1002/jgra.50136>
- Vasko IY, Mozer FS, Krasnoselskikh VV, et al (2018) Solitary waves across supercritical quasi-perpendicular shocks. *Geophys Res Lett* 45(12):5809–5817. <https://doi.org/10.1029/2018GL077835>
- Verscharen D, Chandran BDG, Boella E, et al (2022) Electron-driven instabilities in the solar wind. *Front Astron Space Sci* 9:951628. <https://doi.org/10.3389/fspas.2022.951628>
- Viberg H, Khotyaintsev YV, Vaivads A, et al (2013) Mapping HF waves in the reconnection diffusion region. *Geophys Res Lett* 40:1032. <https://doi.org/10.1002/grl.50227>
- Viberg H, Khotyaintsev YV, Vaivads A, et al (2014) Whistler mode waves at magnetotail dipolarization fronts. *J Geophys Res* 119:2605. <https://doi.org/10.1002/2014JA019892>
- Vogt J, Haaland S, Paschmann G (2011) Accuracy of multi-point boundary crossing time analysis. *Ann Geophys* 29(12):2239–2252. <https://doi.org/10.5194/angeo-29-2239-2011>
- Vörös Z (2011) Magnetic reconnection associated fluctuations in the deep magnetotail: Artemis results. *Non-linear Process Geophys* 18(6):861–869. <https://doi.org/10.5194/npg-18-861-2011>
- Vörös Z, Yordanova E, Graham DB, et al (2019) Mms observations of whistler and lower hybrid drift waves associated with magnetic reconnection in the turbulent magnetosheath. *J Geophys Res Space Phys* 124(11):8551–8563. <https://doi.org/10.1029/2019JA027028>
- Wang R, Lu Q, Kotyaintsev YV, et al (2014) Observation of double layer in the separatrix region during magnetic reconnection. *Geophys Res Lett* 41:4851. <https://doi.org/10.1002/2014GL061157>
- Wang S, Chen LJ, Hesse M, et al (2017) Parallel electron heating in the magnetospheric inflow region. *Geophys Res Lett* 44:4384–4392. <https://doi.org/10.1002/2017GL073404>
- Wang GQ, Zhang TL, Wu MY, et al (2019) Solar wind directional change triggering flapping motions of the current sheet: MMS observations. *Geophys Res Lett* 46(1):64–70. <https://doi.org/10.1029/2018GL080023>
- Wang CP, Liu YH, Xing X, et al (2020) An event study of simultaneous Earthward and tailward reconnection exhaust flows in the Earth's midtail. *J Geophys Res Space Phys* 125(6):e2019JA027406. <https://doi.org/10.1029/2019JA027406>
- Wang S, Chen LJ, Ng J, et al (2021) Lower-hybrid drift waves and their interaction with plasmas in a 3D symmetric reconnection simulation with zero guide field. *Phys Plasmas* 28(7):072102. <https://doi.org/10.1063/5.0054626>
- Wang S, Bessho N, Graham DB, et al (2022a) Whistler waves associated with electron beams in magnetopause reconnection diffusion regions. *J Geophys Res Space Phys* 127(9):e2022JA030882. <https://doi.org/10.1029/2022JA030882>
- Wang S, Chen LJ, Bessho N, et al (2022b) Lower-hybrid wave structures and interactions with electrons observed in magnetotail reconnection diffusion regions. *J Geophys Res Space Phys* 127(5):e2021JA030109. <https://doi.org/10.1029/2021JA030109>
- Wei YY, Huang SY, Rong ZJ, et al (2019) Observations of short-period current sheet flapping events in the Earth's magnetotail. *Astrophys J Lett* 874(2):L18. <https://doi.org/10.3847/2041-8213/ab0f28>
- Wilder FD, Ergun RE, Goodrich KA, et al (2016) Observations of whistler mode waves with nonlinear parallel electric fields near the dayside magnetic reconnection separatrix by the magnetospheric multiscale mission. *Geophys Res Lett* 43:5909–5917. <https://doi.org/10.1002/2016GL069473>
- Wilder FD, Ergun RE, Newman DL, et al (2017) The nonlinear behavior of whistler waves at the reconnecting dayside magnetopause as observed by the magnetospheric multiscale mission: a case study. *J Geophys Res Space Phys* 122(5):5487–5501. <https://doi.org/10.1002/2017JA024062>
- Wilder FD, Ergun RE, Burch JL, et al (2018) The role of the parallel electric field in electron-scale dissipation at reconnecting currents in the magnetosheath. *J Geophys Res Space Phys* 123(8):6533–6547. <https://doi.org/10.1029/2018JA025529>
- Wilder FD, Ergun RE, Hoilijoki S, et al (2019) A survey of plasma waves appearing near dayside magnetopause electron diffusion region events. *J Geophys Res Space Phys* 124(10):7837–7849. <https://doi.org/10.1029/2019JA027060>
- Wilder FD, Conley M, Ergun RE, et al (2022) Magnetospheric multiscale observations of waves and parallel electric fields in reconnecting current sheets in the turbulent magnetosheath. *J Geophys Res Space Phys* 127(9):e2022JA030511. <https://doi.org/10.1029/2022JA030511>
- Winarto HW, Kunz MW (2022) Triggering tearing in a forming current sheet with the mirror instability. *J Plasma Phys* 88(2):905880210. <https://doi.org/10.1017/S0022377822000150>
- Wu M, Volwerk M, Lu Q, et al (2013) The proton temperature anisotropy associated with bursty bulk flows in the magnetotail. *J Geophys Res Space Phys* 118(8):4875–4883. <https://doi.org/10.1002/jgra.50451>
- Wygant JR, Keiling A, Cattell CA, et al (2002) Evidence for kinetic Alfvén waves and parallel electron energization at 4–6 re altitudes in the plasma sheet boundary layer. *J Geophys Res Space Phys* 107(A8):SMP 24–1–SMP 24–15. <https://doi.org/10.1029/2001JA900113>

- Wygant JR, Cattell CA, Lysak R, et al (2005) Cluster observations of an intense normal component of the electric field at a thin reconnecting current sheet in the tail and its role in the shock-like acceleration of the ion fluid into the separatrix region. *J Geophys Res Space Phys* 110:A09206. <https://doi.org/10.1029/2004JA010708>
- Yamada M, Kulsrud R, Ji H (2010) Magnetic reconnection. *Rev Mod Phys* 82:603–664. <https://doi.org/10.1103/RevModPhys.82.603>
- Yao X, Muñoz PA, Büchner J (2022b) Non-thermal electron velocity distribution functions due to 3D kinetic magnetic reconnection for solar coronal plasma conditions. *Phys Plasmas* 29(2):022104. <https://doi.org/10.1063/5.0061151>
- Yao X, Muñoz PA, Büchner J, et al (2022a) Wave emission of nonthermal electron beams generated by magnetic reconnection. *Astrophys J* 933(2):219. <https://doi.org/10.3847/1538-4357/ac7141>
- Yoo J, Jara-Almonte J, Yarger E, et al (2018) Whistler wave generation by anisotropic tail electrons during asymmetric magnetic reconnection in space and laboratory. *Geophys Res Lett* 45(16):8054–8061. <https://doi.org/10.1029/2018GL079278>
- Yoo J, Ji JY, Ambat MV, et al (2020) Lower hybrid drift waves during guide field reconnection. *Geophys Res Lett* 47(21):e2020GL087192. <https://doi.org/10.1029/2020GL087192>
- Yoo J, Ng J, Ji H, et al (2024) Anomalous resistivity and electron heating by lower hybrid drift waves during magnetic reconnection with a guide field. *Phys Rev Lett* 132:145101. <https://doi.org/10.1103/PhysRevLett.132.145101>
- Yoon PH, Lui ATY (2008) Drift instabilities in current sheets with guide field. *Phys Plasmas* 15:072101. <https://doi.org/10.1063/1.2938386>
- Yoon PH, Lui ATY, Sitnov MI (2002) Generalized lower-hybrid drift instabilities in current-sheet equilibrium. *Phys Plasmas* 9(5):1526–1538. <https://doi.org/10.1063/1.1466822>
- Yuan Z, Dong Y, Huang S, et al (2022) Direct observation of acceleration and thermalization of beam electrons caused by double layers in the Earth's plasma sheet. *Geophys Res Lett* 49(13):e2022GL099483. <https://doi.org/10.1029/2022GL099483>
- Zelenyi L, Artemiev A, Malova H, et al (2008) Marginal stability of thin current sheets in the Earth's magnetotail. *J Atmos Sol-Terr Phys* 70(2–4):325–333. <https://doi.org/10.1016/j.jastp.2007.08.019>
- Zhang YC, Lavraud B, Dai L, et al (2017) Quantitative analysis of a Hall system in the exhaust of asymmetric magnetic reconnection. *J Geophys Res Space Phys* 122(5):5277–5289. <https://doi.org/10.1002/2016JA023620>
- Zhang X, Angelopoulos V, Artemyev AV, et al (2018) Whistler and electron firehose instability control of electron distributions in and around dipolarizing flux bundles. *Geophys Res Lett* 45(18):9380–9389. <https://doi.org/10.1029/2018GL079613>
- Zhang X, Angelopoulos V, Artemyev A, et al (2019) Energy transport by whistler waves around dipolarizing flux bundles. *Geophys Res Lett* 46(21):11718–11727. <https://doi.org/10.1029/2019GL084226>
- Zhang H, Zhong Z, Tang R, et al (2022) Observations of whistler-mode waves and large-amplitude electrostatic waves associated with a dipolarization front in the bursty bulk flow. *Astrophys J* 933(1):105. <https://doi.org/10.3847/1538-4357/ac739d>
- Zhang S, Chien A, Gao L, et al (2023) Ion and electron acoustic bursts during anti-parallel magnetic reconnection driven by lasers. *Nat Phys* 19(6):909–916. <https://doi.org/10.1038/s41567-023-01972-1>
- Zhong ZH, Zhou M, Graham DB, et al (2022) Evidence for whistler waves propagating into the electron diffusion region of collisionless magnetic reconnection. *Geophys Res Lett* 49(7):e2021GL097387. <https://doi.org/10.1029/2021GL097387>
- Zhou M, Ashour-Abdalla M, Deng X, et al (2009a) Themis observation of multiple dipolarization fronts and associated wave characteristics in the near-Earth magnetotail. *Geophys Res Lett* 36(20):L20107. <https://doi.org/10.1029/2009GL040663>
- Zhou M, Deng XH, Li SY, et al (2009b) Observation of waves near lower hybrid frequency in the reconnection region with thin current sheet. *J Geophys Res* 114:A02216. <https://doi.org/10.1029/2008JA013427>
- Zhou M, Berchem J, Walker RJ, et al (2018) Magnetospheric multiscale observations of an ion diffusion region with large guide field at the magnetopause: current system, electron heating, and plasma waves. *J Geophys Res Space Phys* 123(3):1834–1852. <https://doi.org/10.1002/2017JA024517>

**Publisher's Note** Springer Nature remains neutral with regard to jurisdictional claims in published maps and institutional affiliations.

## Authors and Affiliations

D.B. Graham<sup>1</sup>  · G. Cozzani<sup>2</sup>  · Yu.V. Khotyaintsev<sup>1,3</sup>  · V.D. Wilder<sup>4</sup> · J.C. Holmes<sup>5</sup> · T.K.M. Nakamura<sup>6</sup> · J. Büchner<sup>7,8</sup> · K. Dokgo<sup>9</sup> · L. Richard<sup>1</sup>  · K. Steinvall<sup>10</sup> 

**C. Norgren**<sup>1,11</sup>  · **L.-J. Chen**<sup>12</sup>  · **H. Ji**<sup>13,14</sup>  · **J.F. Drake**<sup>15</sup>  · **J.E. Stawarz**<sup>16</sup> · **S. Eriksson**<sup>17</sup>

✉ D.B. Graham  
[dgraham@irfu.se](mailto:dgraham@irfu.se)

✉ Y.V. Khotyaintsev  
[Yuri.Khotyaintsev@rymdfysik.uu.se](mailto:Yuri.Khotyaintsev@rymdfysik.uu.se)

- <sup>1</sup> Swedish Institute of Space Physics, Uppsala, Sweden
- <sup>2</sup> Department of Physics, University of Helsinki, Helsinki, Finland
- <sup>3</sup> Department of Physics and Astronomy, Uppsala University, Uppsala, Sweden
- <sup>4</sup> Department of Physics, University of Texas at Arlington, Arlington, TX, USA
- <sup>5</sup> T-5, Los Alamos National Laboratory, Los Alamos, NM, USA
- <sup>6</sup> Space Research Institute, Austrian Academy of Sciences, Graz, Austria
- <sup>7</sup> Max Planck Institute for Solar System Research, Göttingen, Germany
- <sup>8</sup> Centre for Astronomy and Astrophysics, Technical University of Berlin, Berlin, Germany
- <sup>9</sup> Southwest Research Institute, San Antonio, TX, USA
- <sup>10</sup> Department of Physics, Chalmers University of Technology, Göteborg, Sweden
- <sup>11</sup> Departement of Physics and Technology, University of Bergen, Bergen, Norway
- <sup>12</sup> NASA Goddard Space Flight Center, Greenbelt, MD, USA
- <sup>13</sup> Department of Astrophysical Sciences, Princeton University, Princeton, NJ, USA
- <sup>14</sup> Princeton Plasma Physics Laboratory, P.O. Box 451, Princeton, NJ, USA
- <sup>15</sup> Department of Physics, Institute for Physical Science and Technology and Joint Space Science Institute, University of Maryland, College Park, MD, USA
- <sup>16</sup> Northumbria University, Newcastle upon Tyne, UK
- <sup>17</sup> Laboratory for Atmospheric and Space Physics, University of Colorado, Boulder, CO, USA